REVIEW

Check for updates

Factors influencing self-trapped exciton emission of low-dimensional metal halides

Ying Han,†[ab] Xiaohua Cheng [iD] †[ab] and Bin-Bin Cui [iD] *[abc]

Organic–inorganic hybrid metal halides (MHs) are widely used in the field of photoelectricity due to their excellent structure and photoelectric tunability. When separating inorganic metal halides by larger organic cations in crystals, multiple low-dimensional MHs (LDMHs) at the molecular level can be constructed, including two-dimensional (2D) layers, one-dimensional (1D) chains, and zero-dimensional (0D) clusters assembled by octahedral metal halide units. These LDMHPs exhibit significantly different luminescence properties from 3D MHs, which stem from the radiative recombination of self-trapped excitons (STEs) or the defect states. Along with the structure dimensions, the degree of intrinsic and instantaneous structure distortions greatly affects the STE broadband emission of LDMHs. Furthermore, molecular engineering such as the choice of organic cations, electron–phonon coupling effect, external temperature and pressure, and metal ion doping can greatly change the luminescence properties of LDMHs. Herein, we summarize and discuss the factors influencing the STE emission of LDMHs for a better understanding and to prospect the development of LDMHs in future.

1. Introduction

Organic–inorganic hybrid metal halides (MHs) have been widely applied in optoelectronic devices for their unique, multiple, and tunable structures,[1] as their dimensions and intrinsic structures can be regulated by rational design with components.[2] As shown in Fig. 1, replacing methylammonium (MA$^+$), formamidine (FA$^+$), and/or cesium (Cs$^+$) in three-dimensional (3D) metal halides by larger organic cations in size can build multiple low-dimensional MHs (LDMHs) at the molecular level,[3] such as two-dimensional (2D) layers, one-dimensional (1D) chains, and zero-dimensional (0D) metal halide octahedral clusters.[4] LDMHs have opened a new frontier in photodetector,[5] scintillator,[6] laser,[7] single component phosphor,[8] and light emitting diode (LED) devices[9] for excellent luminescence and high photoluminescence quantum efficiency (PLQE).[10] Traditional 3D lead halide perovskites usually show narrow emissions.[11] On the contrary, LDMHs exhibit typical luminescent properties of large Stokes shift and broadband emission, which is usually attributed to the radiative recombination of self-trapped excitons (STEs).[12] The soft nature of the LDMHs make ultrafast structural distortion easier upon optical excitation.[13] The formation of STEs is due to the strong

electron–phonon coupling in the distortion-induced lattices, which generates small polarons binding the excitons under excitation.[14] While the luminescence mechanism of the broadband emission in regular 100-oriented 2D MHs is still under debate. In addition to STE states emission, the defect-induced broadband emission has recently been reported in (BA)$_2$PbBr$_4$[15] and (PEA)$_2$PbI$_4$[16] 2D perovskite crystals.

Generally, the degree of the intrinsic inter-octahedral and/or individual intra-octahedral distortions are related to the broadband emission of the self-trapping states.[17] Inter-octahedral distortion can be divided into out-of-plane distortion and in-plane distortion. The photoluminescence (PL) intensity of the broad emission increases linearly with increasing out-of-plane distortion degree,[18] and the lead-halide octahedral intra-octahedral distortion has a linear relationship with the full width at half-maximum (FWHM) of the PL emission, showing the dependency of STE emission on the structure distortion.[19] In addition, instantaneous structure distortion after being excited has a great influence on STE states and emission.[20] Structure distortion can be regulated by reasonably choosing chemical compositions, which influence the photoelectric properties of LDMHs. Molecular engineering, such as the choice of organic cations, can also directly regulate the photoluminescence characteristics of LDMHs.[21] The energy level of organic cations relative to that of inorganic frameworks can be regulated by adjusting organic molecules, which result in different types of emissions with different mechanisms.[22] It is worth mentioning that the vibration of organic cations that are not isolated from the inorganic cage and the regulation of

^{a} *Advanced Research Institute of Multidisciplinary Science, Beijing Institute of Technology (BIT), Beijing 100081, P. R. China. E-mail: cui-chem@bit.edu.cn*

^{b} *School of Chemistry and Chemical Engineering, BIT, Beijing 100081, P. R. China*

^{c} *School of Materials Science and Engineering, BIT, Beijing 100081, P. R. China*

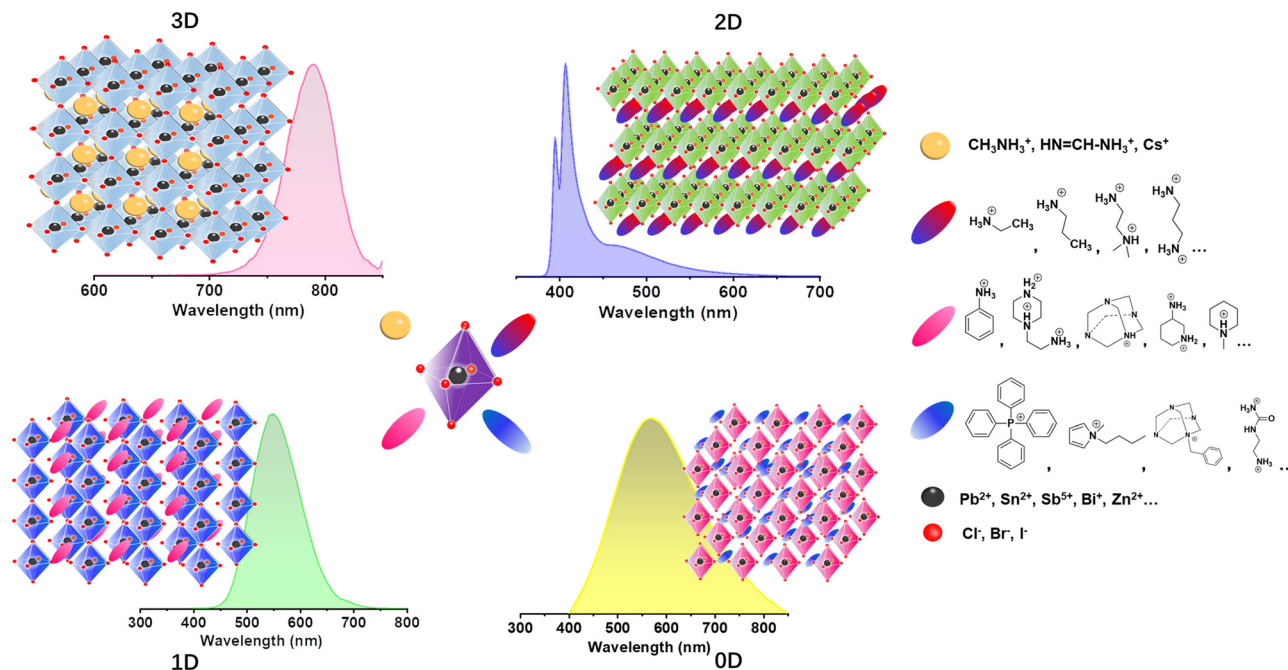† Y. H. and X. C. contributed equally to this work.

Fig. 1 Typical structures of 3D, 2D, corrugated 2D, 1D, and 0D MHs and their typical photoluminescence spectra, respectively.

organic cations can effectively tune the electron–phonon coupling strength.[23]

Furthermore, the configuration of some LDMHs that changes with ambient temperature and pressure will produce structure transition and greatly change the photophysical and photoelectric properties of LDMHs.[11] For example, pressure-induced emission (PIE) has been found in some LDMHs, such as 1D EAPbI$_3$,[24] C$_4$N$_2$H$_{14}$SnBr$_4$,[25] and 2D (PEA)$_2$PbBr$_4$,[26] (BA)$_4$AgBiBr$_8$[27] perovskite crystals. In addition, doping metal ions can tune the luminescence properties and efficiently enhance the luminescence of LDMHs. For example, divalent Mn^{2+} can introduce intermediate energy level emission and greatly improve PLQE.[28] Other doping metal elements in LDMHs have also been investigated, such as Sb^{3+},[29] Bi^{3+},[30] and Sn^{2+}.[31]

In conclusion, the structure distortion, molecular engineering of organic cations, electron–phonon coupling strength, external temperature and pressure, and metal ion doping will greatly affect the STE broadband emission of LDMHs. However, the generalization and summarization of the role of these factors on self-trapped excitons of LDMHs are still not systematic enough. In this work, we mainly introduce and discuss these factors influencing the STE emission of LDMHs, which will help us to better design LDMH materials with specific and photoelectric functions.

2. The STE broadband emission mechanism

Unlike 3D metal halide perovskites and most regular 100-oriented 2D structures with small Stokes shifts and narrow FWHM, 0-1D MHs,[32] 110-oriented corrugated 2D MHs,[12a,b,33] some distorted 100-oritented 2D MHs[12c,33,34] usually have broadband emissions with large Stokes shifts, and usually white emissions covering the entire spectrum at room temperature. Here, the difference lies in that the 3D perovskite material under excitation generates large-area polarons[35] (Fig. 2(a)), which exhibit long-range distortion of the lattice. However, when the LDMHs are excited, Pb–X bonds are easily deformed to generate small polarons and trap excitons.[36] As shown in Fig. 2(b), when the Pb–Pb bonds are shortened, the photogenerated electrons are captured at the Pb–Pb site, and the Pb–Pb dimer couples with photogenerated electrons to form Pb$_2^{3+}$. Similarly, when the X–X bands are shortened, holes are trapped to form X$_2^-$ and when Pb–X bonds are shortened, holes are located on a single Pb atom, resulting in the formation of Pb^{3+} centers.[38] Therefore, an intermediate energy STE states for trapping electron and holes is introduced into the forbidden band[39] (Fig. 2(c)). The STE level has a wide energy distribution, which results in broadband emission with a large Stokes shift of LDMHs.[40] It is worth mentioning here that for the 0D MHs, the single lead-halide octahedrons are completely isolated by organic cations (Fig. 2(d)). The excitons are completely confined to the isolated individual octahedron and there is no coupling effect.[41] The mechanism of broadband emission from 0D MHs is shown in Fig. 2(e), which a significant change in the charge distribution compared to the ground state upon excitation causes changes in the bond length and bond angle of the individual octahedron, in turn leading to excited-state structural reorganization.[37] The reorganized excited states have wide energy distribution energy related to the degree of structural distortion, which results in the broadband emission of 0D MHs.[42]
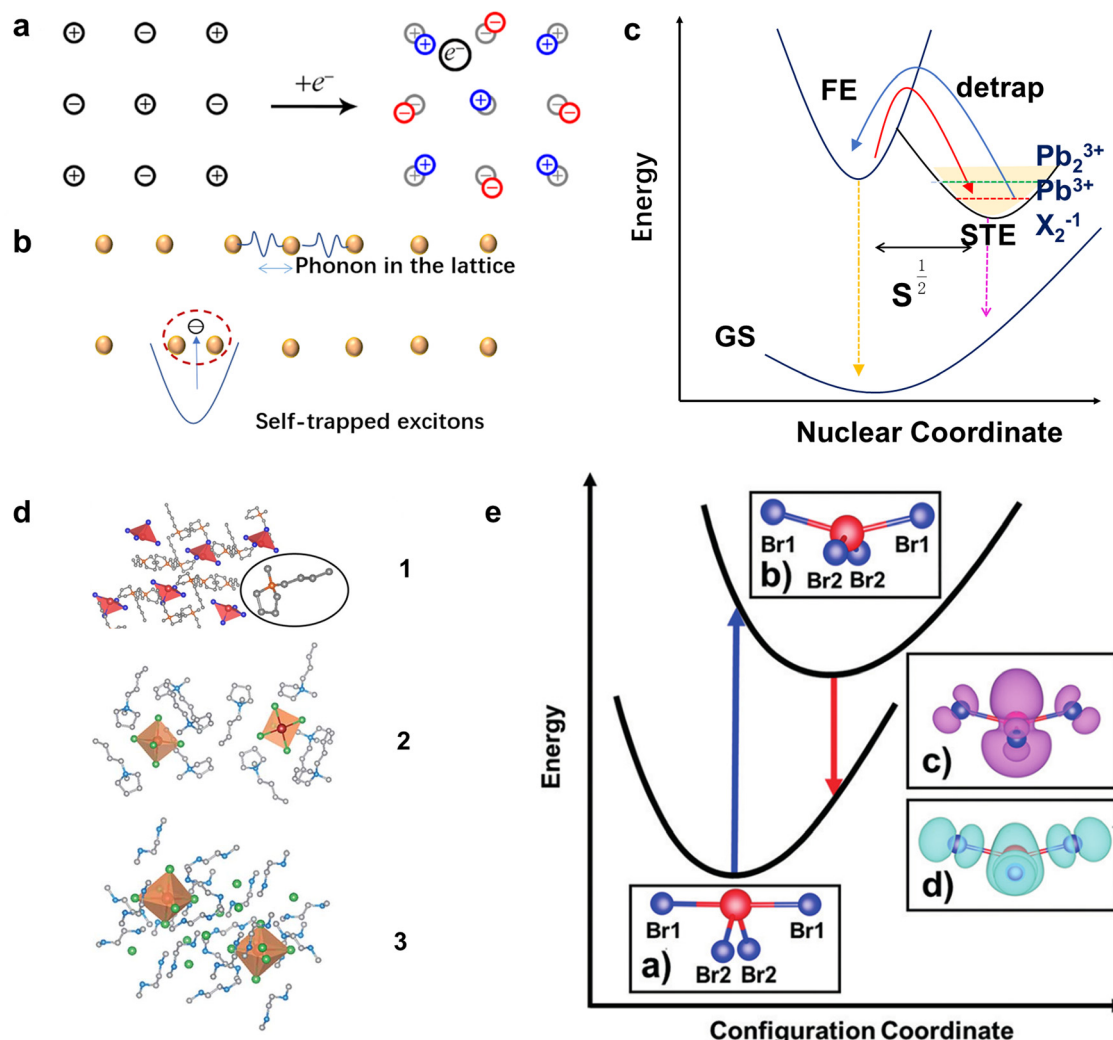
Fig. 2 (a) Schematic diagram for the formation of large polarons in the lattice of a 3D material excited by light. Reproduced with permission.[36] Copyright 2018 American Chemical Society. (b) Schematic diagram of the Pb–Pb dimer couples with photogenerated electrons to form Pb_2^{3+} in LDMHs. (c) Graphs of low-dimensional perovskite excitons self-trapping (blue) and detrapping (red) (GS = ground state, FE = free exciton state, STE = self-trapped exciton state, pink, and black downward arrows indicate FE and STE photoluminescence, respectively). (d) The 0D structures are completely isolated by organic cations. Reproduced with permission.[37] Copyright 2018 Wiley-VCH. (e) Configuration coordinate diagram of the large Stokes displacement caused by the deformation of the excited state structure of 0D structures. Reproduced with permission.[37] Copyright 2018 Wiley-VCH.

Furthermore, the origin of the broadband emission in 100-oriented 2D MHs is still controversial, and there are two mechanisms. In addition to the explanation of the broadband emission by the STE mechanism, some recent studies and evidence suggest that such emission may also be caused by the defect states rather than STE states. For example, Zhang *et al.*[16] showed that the broadband emission intensity of $(PEA)_2PbI_4$ can be adjusted by tuning the concentration of excess iodine during crystal growth. As shown in Fig. 3(a), the crystal 0.157 I-PEPI exhibits yellowish emission, which is distinct from the green emission of typical 0I-PEPI crystals. 0I-PEPI show a sharp emission, while 0.157I-PEPI show a dominant broadband emission (Fig. 3(b)). The broadband emission shows an increasing ratio with increasing iodine ion concentration (Fig. 3(c)). In this case, the authors suggest that broadband emission originates from iodine interstitials. In addition,

Park *et al.*[15] found that the PL intensities of broadband emission in the $(BuA)_2PbBr_4$ crystal were proportional to the thickness (Fig. 3(d)). They predicted that the broadband emission may originate from defect radiative recombination, *i.e.*, the organic cation vacancies generated by intercalated water molecules (Fig. 3(e)).

Kahmann *et al.* made a distinction between the two mechanisms, as shown in Fig. 4(a), wherein STEs are formed by transient lattice deformation after excitation, and therefore, only the above-gap excitation can lead to STE luminescence. However, the defect states can also be excited directly by excitation energies lower than the bandgap.[43] They performed the PL spectrum of PEA_2PbI_4 excited by below-bandgap photons. As shown in Fig. 4(b), identical broadband emission using excitation energy from 2.07 to 2.48 eV proves that the broadband emission originates from defects. Furthermore,
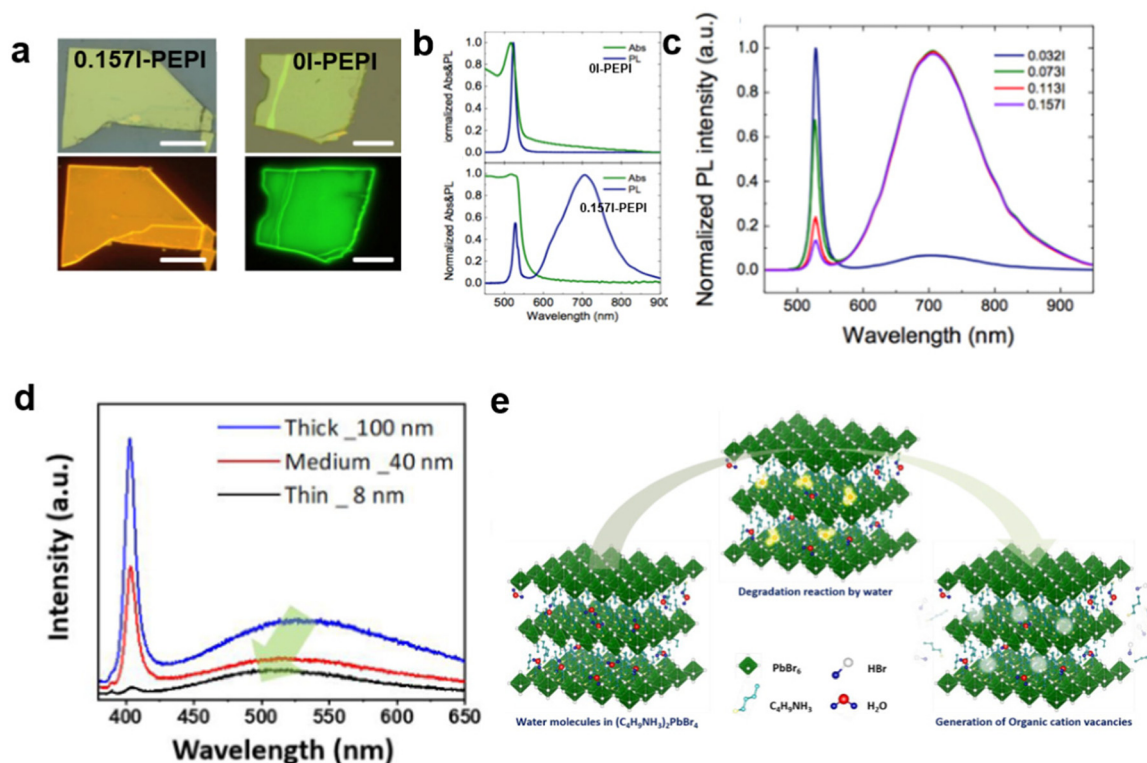
Fig. 3 (a and b) Optical micrograph and corresponding fluorescence images under excitation for 0.157I-PEPI and 0I-PEPI crystals.[16] (c) UV–vis Abs and PL spectra of 0I-PEPI flakes and 0.157I-PEPI flakes. Reproduced with permission.[16] Copyright 2019 American Chemical Society. (d) PL spectra of the OHP depending on the thickness.[15] (e) Schematic of the water-assisted degradation mechanism in (BuA)$_2$PbBr$_4$ microsheets. Reproduced with permission.[15] Copyright 2019 American Chemical Society.

Yin et al.[44] experimentally and theoretically demonstrated that the broadband emission in PEA$_2$PbI$_4$ originates from the iodine vacancies defect luminescence centers (Fig. 4(c)). As shown in Fig. 4(d), for 2D PEA$_2$PbI$_4$ crystals treated by excess PEAI, the intensity of broadband emission was largely reduced as the PEAI treatment plays a key role in the passivation of I vacancies of the single crystals. It is worth mentioning that for the tin-based 100-oriented 2D MHs, it is easier to produce strong STE emission rather than defect-induced emission. For example, Deng et al.[45] reported the 2D tin halide perovskite, which exhibited STE emission with a large Stokes shift and broad bandwidth. It displayed a high PLQE of near-unity in the solid-state and showed excellent stability.

In our scenario, the broadband emission reported to be from self-trapping states need to be verified by further post-treatments, such as acetone[46] or cationic salts solution[44] ultrasound. In addition, the ratio of organic amine to lead oxide (PbO) needs to be changed during synthesis, and the single crystals grown can be recrystallized to eliminate defects.

3. Factors influencing STE broadband emission

3.1. Structure distortion

To date, materials with broadband emission are mostly 1D,[47] 0D,[32b,48] and corrugated 110-oriented 2D MHs.[12] Most

100-oriented 2D perovskites show emission with a narrow peak, and a few distorted 100-oriented 2D perovskites exhibit STE broadband emission.[34,49] Previous papers consistently reported that the STE emission of 100-oriented perovskites are related to the degree of inter-octahedral distortion of the inorganic layer and intra-octahedral distortion of individual octahedrons.[49,50] The inter-octahedral distortion (Fig. 5(a)) can be divided into two types—out-of-plane distortion (Fig. 5(b)) and in-plane distortion (Fig. 5(c)).[18] The in-plane distortion is that the Pb–Br–Pb bond angle parallel to the 2D layer deviates from 180 degrees, which is recorded as θ_{in}, $D_{in} = 180° - \theta_{in}$. Out-of-plane distortion refers to distortion perpendicular to the direction of the layer, which is denoted as θ_{out}, $D_{out} = 180° - \theta_{out}$. It has recently been verified that the emission intensity of 100-oriented 2D structures is directly related to out-of-plane distortion. As shown in Fig. 5(d), the increasing D_{out} correlates linearly with the increasing intensity of STE broadband emission.

As for the intra-octahedral distortion of individual octahedrons, the calculation formula is as follows

$$\Delta d = \frac{1}{6} \sum \left[\frac{d_n - d}{d} \right]^2$$

where d represents the average bond length of Pb–Br, d_n are six individual Pb–Br bond lengths of a single octahedron, and Δd_{avg} is the average of Δd. Kanatzidis' group[19] reported the relationship between the distortion of lead-halide octahedral
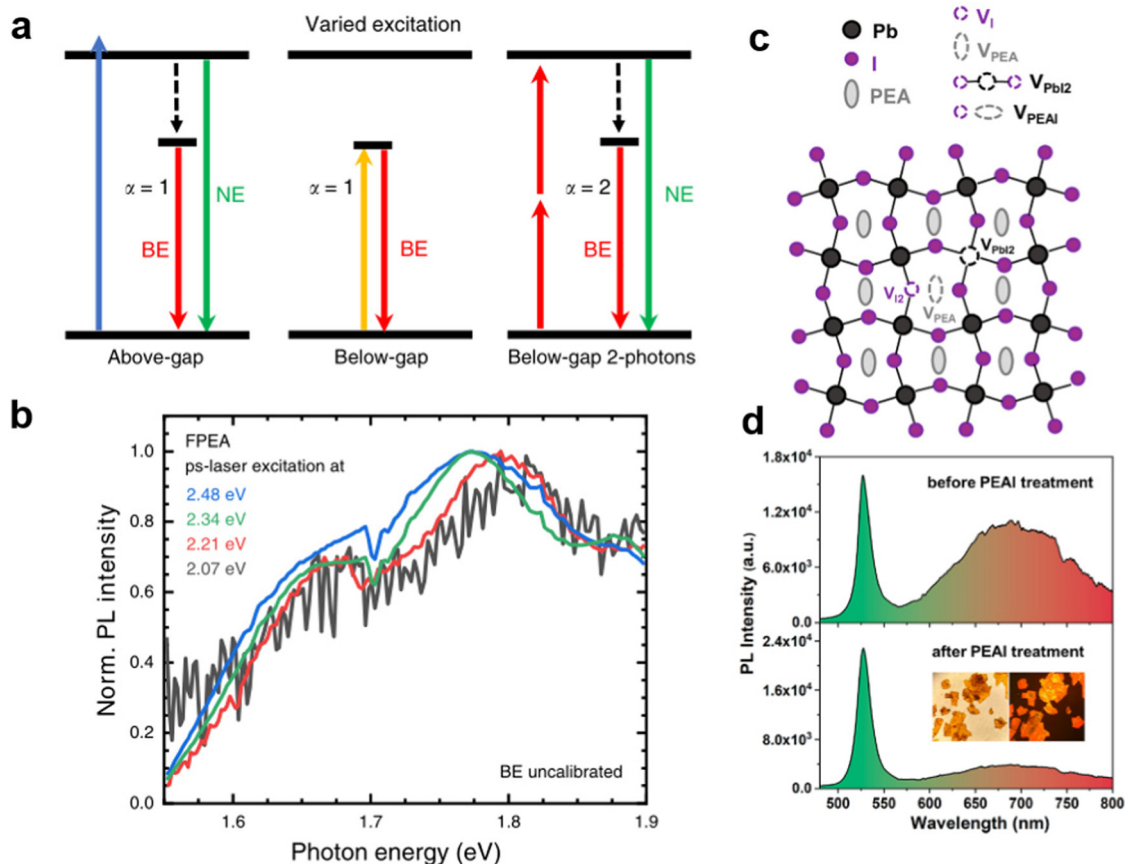
Fig. 4 (a) Two-photon excitation scales of above-gap and below-gap energy.[43] (b) The broad emission can be excited using below-gap photons. Reprinted with permission.[43] Copyright 2020 Springer Nature. (c) Schematic illustration of point defects (V_I, V_{PEA}, V_{PbI_2}, and V_{PEAI}) of PEA_2PbI_4.[44] (d) PL spectra of the PEA_2PbI_4 before and after PEAI treatment. Reprinted with permission.[44] Copyright 2020 American Chemical Society.

and FWHM. They prepared three types of 2D materials with different degrees of distortion by regulating the organic cations, α-(DMEN)PbBr$_4$, (DMAPA)PbBr$_4$, and (DMABA)PbBr$_4$. It was found that the average distorted degree of lead-halide octahedron is linearly related to the FWHM of the PL emission, *i.e.*, the greater the degree of distortion, the wider the FWHM. Recently, J. England *et al.*[51] further reported the dependency of STE broadband emission on individual intra-octahedral distortion. They synthesized two 100-oriented 2D perovskites with almost no out-of-plane distortions. With large intra-octahedral distortions, these two 100-oriented 2D perovskites thus exhibit STE-based broadband emission.

In addition, some other researchers regulated the structure distortion by regulating the halogen to achieve broadband white light emission.[52] For example, EA$_4$Pb$_3$Cl$_{10}$ with a large distortion shows broadband white emission, while EA$_4$Pb$_3$Br$_{10}$ with a small distortion shows narrow blue emission.[53] By further adjusting the Cl/Br ratio for EA$_4$Pb$_3$Br$_{10-x}$Cl$_x$ ($x = 0, 2, 4, 6, 8, 9.5, 10$), they found that two compounds ($x = 8$ and 9.5) have more optimized white emissions than pure EA$_4$Pb$_3$Cl$_{10}$ (Fig. 5(e)). Aymen Yangui *et al.*[54] realized white-light emission from the mixed 2D hybrid perovskites $(C_6H_{11}NH_3)_2[PbBr_{4-x}I_x]$ and studied the FWHM of PL increasing with the bromine

content (Fig. 5(f)), which was excellently correlated with the change in the angular distortion in inorganic octahedral PbX$_6$ (X = I/Br).

It is worth mentioning that instantaneous structure distortion under excitation also has a great influence on STE emission. For example, Ye *et al.*[20] reported that broadband emission shows strong dependence on the molecular conformational of organic cations. They synthesized a series of 2D perovskites with different lengths ($[CH_3(CH_2)_{n-1}NH_3]_2PbI_4$, $n = 4, 6, 8, 10, 12, 18$). With the increase in the cationic chain length, the chain distortion of organic cations is easy under excitation, which induces polaron formation and charge-carrier trapping. As shown in Fig. 6(a), as the organic cations chain length increases, the charge-carrier mobility initially increases ($n \leq 6$) and then decreases ($n \geq 6$). As illustrated in Fig. 6(b), there is a relationship between the low charge-carrier mobility and broadband emission. After the free carriers are relaxed to free excitons, the self-trapped excited states with different energies will gradually form in the bandgap. As shown in Fig. 6(c), the ratio of the PL intensity of broadband emission to narrow emission (I_{BE}/I_{NE}) decreased with increasing temperature. Fig. 6(d) plots the I_{BE}/I_{NE} ratio at 80 K against the organic cations chain length with different *n* values.
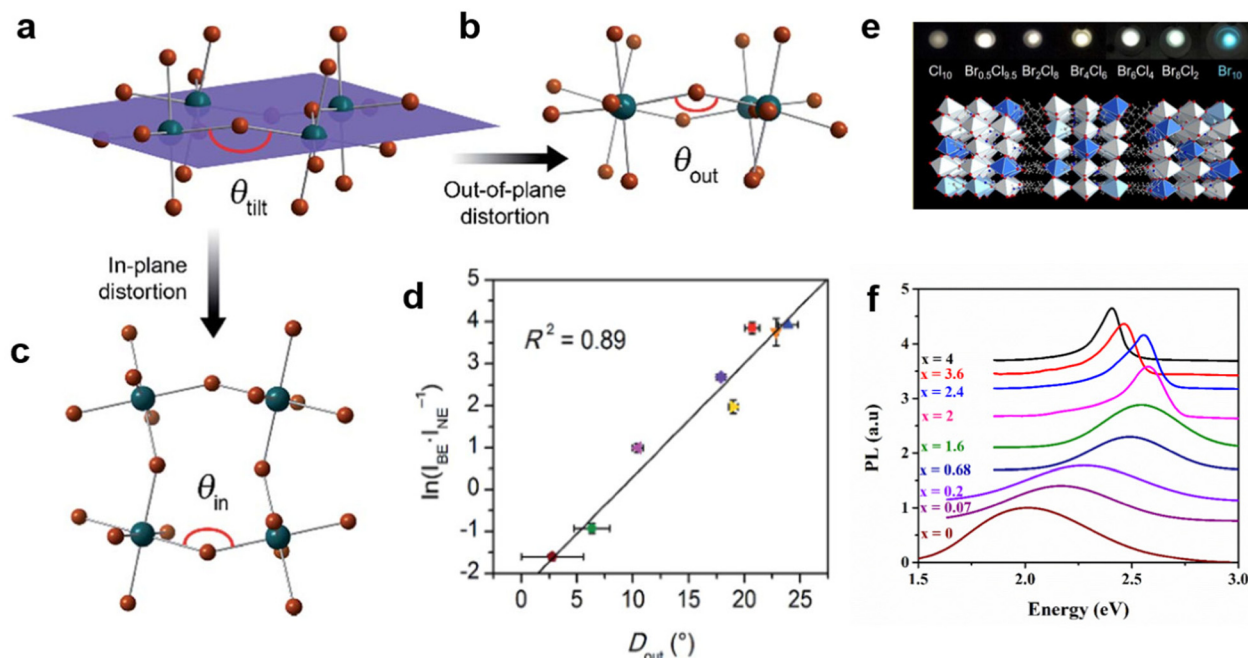
Fig. 5 (a) Schematic diagram of the octahedral tilt decomposition into two parts: out-of-plane distortion (b) and in-plane distortion (c). (d) Relationship between $\ln(I_{BE}/I_{NE})$ and D_{out}. Reproduced with permission.[18] Copyright 2017 The Royal Society of Chemistry. (e) The mixed halogen $EA_4Pb_3Br_{10-x}Cl_x$ ($x =$ 0, 2, 4, 6, 8, 9.5, 10) crystals. Reproduced with permission.[53] Copyright 2019 American Chemical Society. (f) PL of $(C_6H_{11}NH_3)_2[PbBr_{4-x}I_x]$ varies with the content of I. Reproduced with permission.[54] Copyright 2017 Elsevier B.V.
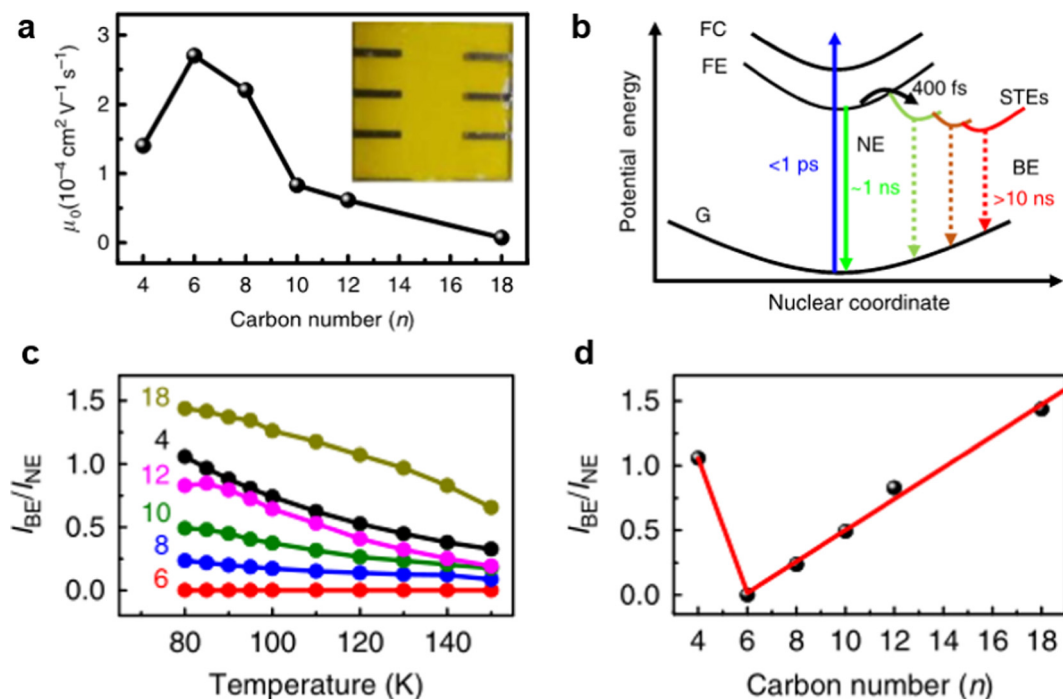

Fig. 6 (a) Out-of-plane charge-carrier mobility varies with n value curves. (b) Schematic of the adiabatic potential energy curves of the ground state (G), free-exciton state (FE), free-carrier state (FC), and various self-trapped excited states (STEs). The vertical dashed line shows possible nonradiative decay processes of the FE and STEs. (c) The I_{BE}/I_{NE} ratio of six samples as a function of temperature ranging from 80 K to 150 K. (d) The I_{BE}/I_{NE} ratio at 80 K is plotted against the alkyl chain length of organic cations. Reprinted with permission.[20] Copyright 2020 Springer Nature.

It was found that the ratio increases with increasing organic cation chain length ($n \geq 6$), which suggests that instantaneous organic chain distortion is conducive to broadband emission.

3.2. Molecular engineering

These LDMHs structures can be regulated by the size of organic cations.[55] For example, for the 2D perovskite $(R_nNH_3)_2MX_4$ and $(NH_3R_nNH_3)MX_4$ constructed by monoamine and diamine organic cations, as shown in Table 1, when $n = 1$, methylamine cation constructs traditional 3D perovskites,[56] and when $n \geq 2$, 2D perovskites are formed.[53] While for $(NH_3R_nNH_3)MX_4$, when $n \geq 4$, regular 100-oriented 2D perovskites can be formed due to the sufficiently long diamine organic cations.[57] As shown in Fig. 7(a) and Table 1, in the formation of butylenediamine ($n = 4$), propylene enediamine ($n = 3$), and ethylenediamine ($n = 2$), as the length of the amine chain is reduced, the layered perovskite changes from a flat layer to a distorted layer, then when $n = 2$, the layer is broken up to construct a 1D structure, resulting in emission transition from a narrow emission to a STE broadband emission.[58] In addition, the cation length also influences the connection styles of the inorganic skeleton. As shown in Fig. 7(b), PMA and PEA organic cations constructed the corner-sharing 2D structures, while the longer PPA and PBA cations constructed corner-sharing and face-sharing coexistent 2D structures.[59]

Furthermore, by the hydrogen bonding force of organic cations, corrugated 110-oriented 2D perovskites can be constructed. The H atoms on the primary and secondary amines of organic cations forms hydrogen bonding with bromine atoms. Therefore, the inorganic layer can be folded $\sim 90°$ to form a corrugated structure (Fig. 7(c)), such as (N-MEDA)[PbBr$_4$],[12c] α-(DMEN)PbBr$_4$,[19] and (epz)PbBr$_4$.[60] Cui et al.[32b] also reported the transition from the 1D to 0D structure by regulating the hydrogen bonding, and the dimension reduction from 1 to 0D increased the PLQE five times from the STE states. Recently, Xing et al.[61] reported the atomic substitution strategy to facilitate the formation of STEs in 2D perovskites. As shown in Fig. 7(d), perovskite crystals are synthesized by halogen-substituted phenyl molecules. The halogen substituent can promote exciton self-trap, resulting in STE broadband emission.

Engineering organic cations can not only tune the intrinsic structures of LDMHs but also play a key role in determining their optical features. Different types of emission can be achieved by regulating the energy levels of different organic cations. The relative level of the LUMO, HOMO energy level of organic cations, and the CBM and VBM of the inorganic framework can be regulated by adjusting organic molecules. For example, Dou et al.[22] demonstrated that the organic and inorganic building blocks of hybrid perovskite materials can be manipulated in a modular fashion to produce widely tunable single crystalline quantum wells. As shown in Fig. 8, there are different types of energy transfer, type 1 is the emission type of most perovskite materials. The energy level of inorganic skeleton is below that of organic molecules, thus showing efficient narrow band emission of inorganic skeleton, and the (ii), (iii), (iv) type realized that the inorganic layer transfers energy to the organic cations, which results in the broadband emission from the organic molecules of these perovskite materials.

For some LDMHs, white-light emission can be attributed to the synergetic effects of the self-trapped excitons and organic component.[62–64] For example, Luo et al.[65] reported a white-light emissive 1D hybrid perovskite, $C_5H_{14}N_2PbCl_4 \cdot H_2O$ (Fig. 9(a)), and they proved that the white-light emission was derived from the synergy of the organic part and self-trapped exciton. As shown in Fig. 9(b), the material exhibits different emission characteristics at different excitation wavelengths, and there are two emission peaks when excited by 344 nm: the narrow emission located at 412 nm is from the $C_5H_{14}N_2Cl_2$ organic part and the broad emission centered at 617 nm is from self-trapped excitons of the inorganic skeleton. We can see from the photoluminescence photographs and CIE chromaticity coordinates that the broadband white emission is produced by the combination of cations with blue light and inorganic components with yellow light. Guo et al.[66] also synthesized two crystalline hybrids $(H_2DABCO)(Pb_2Cl_6)$ and $(H_3O)(Et_2\text{-}DABCO)_8(Pb_{21}Cl_{59})$; the structures are shown in Fig. 9(c). These materials also exhibit the cooperative luminescence of the organic and inorganic part (Fig. 9(d)).

3.3. The electron–phonon coupling effect

It is worth mentioning that the regulation of organic cations greatly affects the electron–phonon coupling of the materials,[67] which has a significant impact on PLQE,[23] FWHM,[68] PL emission peak,[69] hot-carrier cooling,[70] STE broadband emission,[71] etc. The organic cations affect the rigidity of perovskite materials, which further significantly affects the electron–phonon coupling strength. Sargent's group[23] compared the 2D perovskites PEA$_2$PbBr$_4$ and BA$_2$PbBr$_4$ (Fig. 10(a)), and PEA$_2$PbBr$_4$ has higher crystal rigidity due to the lower conformational freedom of organic cations, which leads to weak electron–phonon coupling strength. Fig. 10(b) shows the Raman spectra of PEA$_2$PbBr$_4$ and BA$_2$PbBr$_4$; the BA$_2$PbBr$_4$ Raman spectrum is several times more intense than that of BA$_2$PbBr$_4$, indicating the stronger electron–phonon coupling strength, which enhances the non-radiative recombination rates, resulting in very low PLQE, while the PEA with large rigidity has a high PLQE of 79%. In addition, the cation stacking pattern affects the microstrain, which has been reported by Du et al.[72] As

Table 1 The structures of monoamine $R_nNH_3^+$ and diamine $NH_3R_nNH_3^{2+}$ organic cations

Monoamine organic cations ($R_nNH_3^+$)	Dimension
H_3C—$NH_3 \oplus$ $n=1$	3D
H_3C\\NH_2 $n=2$	2D
H_3C\\\\NH_2 $n=3$	2D

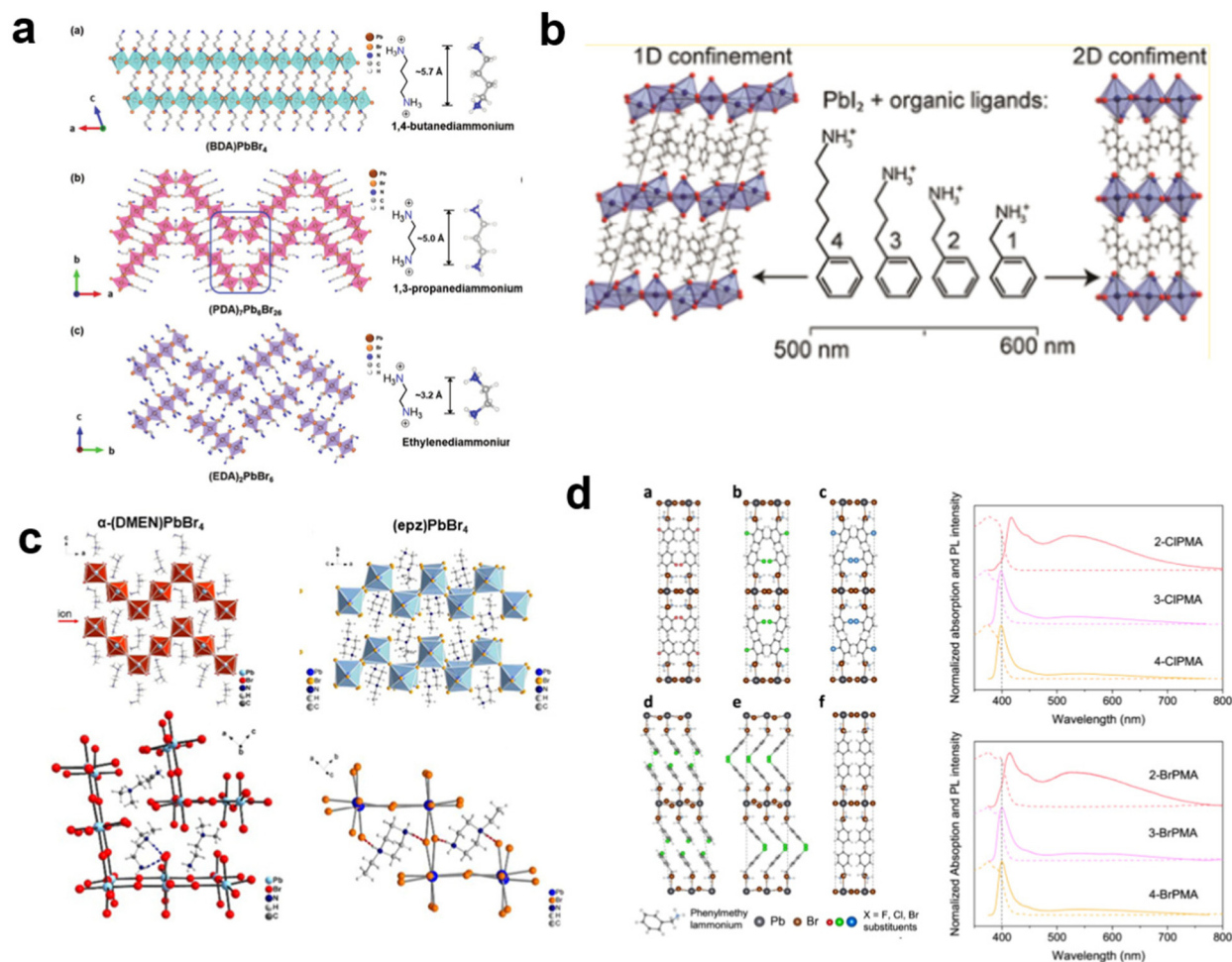| Diamine organic cations ($NH_3R_nNH_3^{2+}$)	Dimension
H_3N\\\\\\NH_3 $n=4$	2D
H_3N\\\\$NH_3 \oplus$ $n=3$	2D
$H_3N \oplus$\\$NH_3 \oplus$ $n=2$	1D

Fig. 7 (a) Views of the structures of 2D and 1D perovskites. Reproduced with permission.[58] Copyright 2020 Wiley-VCH. (b) The 2D structures with corner-sharing, corner-sharing, and face-sharing coexistence. Reproduced with permission.[59] Copyright 2016 American Chemical Society. (c) Structures of corrugated 2D perovskite and hydrogen bonding diagram. Reproduced with permission.[19] Copyright 2017 American Chemical Society and[60] Copyright 2018 American Chemical Society. (d) The 2D perovskites with halogen-substituted organic cations and their PL spectrum. Reproduced with permission.[61] Copyright 2021 Springer Nature.

shown in Fig. 10(c), the FWHM of the XRD peaks increased monotonously with decreasing cation rigidity. A large microstrain leads to strong electron–phonon coupling, which is responsible for the widening of the emission peak (Fig. 10(d)). The 2D perovskite crystals usually shows dual peaks, such as PEA_2PbBr_4, OA_2PbBr_4, and BA_2PbBr_4. Many reports consistently proved that the low-energy peak is from the bulk phase, and the high-energy peak is from a distorted surface phase. Recently, F. Nogueira et al.[69] studied the dual bands emission of the well-known $(BA)_2PbI_4$ (Fig. 10(e)). They found the phonon energy that is quite consistent with the vibration of organic cations in the Raman and infrared spectra (Fig. 10(f)). These vibrational modes transformed from the organic cations to the inorganic layer, resulting in strong electron–phonon coupling and dual band emission.

In addition, the hot carrier cooling rate is closely related to the electron–phonon coupling strength. The cooling process of hot carriers is shown in Fig. 11(a); immediately upon photo-excitation, the hot charge carriers are injected into all the

perovskite QWs and then cool to the band edge states. The strong electro-acoustic coupling effect is beneficial for accelerating carrier cooling and decreasing the cooling rate to a 'hot phonon bottleneck effect'.[70c] Therefore, for the perovskite material, the electron–phonon coupling strength can be changed by regulating the cations, thereby affecting the cooling rate of hot carriers. For example, Zhang et al.[73] studied the different impacts of spacer layer BA cations confined by the 2D framework and MA cations confined by 3D framework have charge carrier dynamics in the two systems. They found that 2D $(BA)_2(MA)Pb_2I_7$ has a faster hot carrier decay rate than that in 3D $MAPbI_3$ due to the stronger nonadiabatic couplings (Fig. 11(b)). Yin et al.[74] also studied the hot carrier cooling process of three single-crystal 2D hybrid perovskite systems (Fig. 11(c)). As shown in Fig. 11(d), they found that $(EA)_2PbI_4$ with weak electron–phonon coupling has a longer hot carrier cooling time compared to that of $(AP)_2PbI_4$ and $(PEA)_2PbI_4$. Therefore, reducing the vibrational coupling between the organic cations and the inorganic framework by changing the
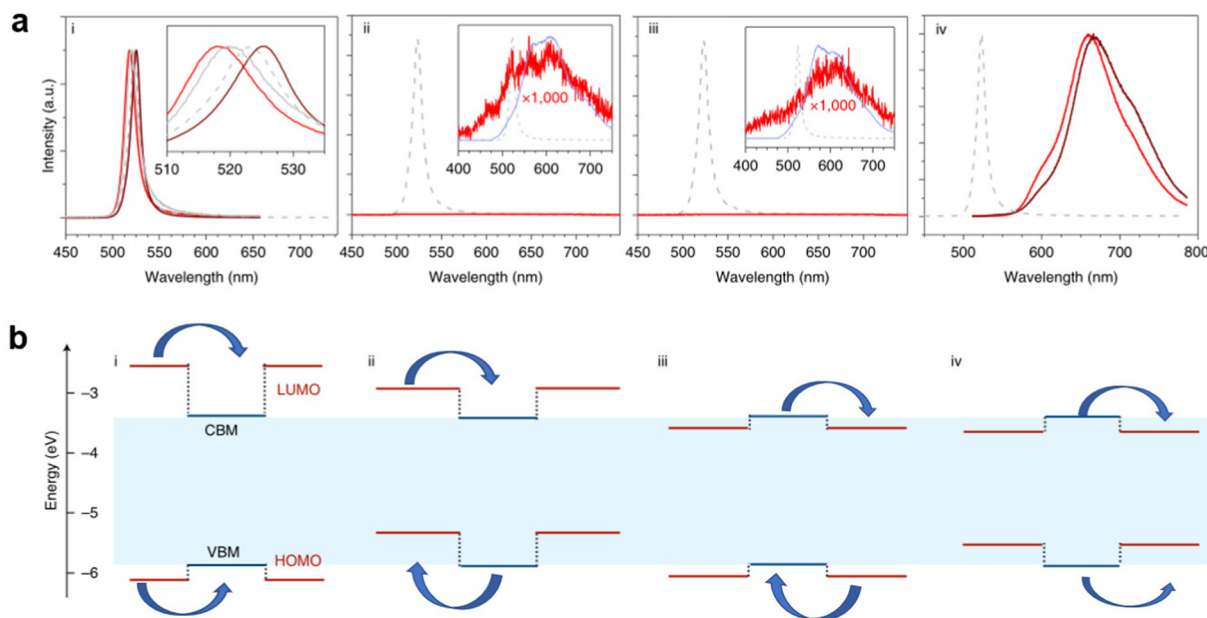
Fig. 8 (a) Corresponding diagram (i), (ii), (iii), (iv) emission spectra of four different types of quantum traps, where the low-energy broad peak comes from organic molecules. (b) Four types of quantum wells constructed by the relative changes in the LUMO HOMO energy level of organic molecules and the CBM and VBM of inorganic frameworks (VBM, valence band maximum; CBM conduction band minimum; HOMO, highest occupied molecular orbital; LUMO, lowest unoccupied molecular orbital). Reprinted with permission.[22] Copyright 2020 Springer Nature.

functional groups of the organic spacer cations has the potential to slow down the hot carrier relaxation and increase the carrier lifetime, thereby improving the PCE of solar cells.

Furthermore, the formation of an STE depends strongly on electron–phonon coupling to induce small polarons in the local lattice.[14] Recently, Chen et al.[75] reported the two 100-oriented 2D perovskites $(C_7H_7N_2)_2PbX_4$ (X = Cl, Br) with two different halogens. Interestingly, the two perovskite crystals show different emission mechanisms even with a similar monolayer crystal structure, which are almost deformation-free in the inorganic octahedral framework (Fig. 11(e)). As shown in Fig. 11(f), the halogen substitution from Cl^- to Br^- results in a 10-fold enhancement of the electron–phonon coupling that affects the dynamics of STE. $(C_7H_7N_2)_2PbBr_4$ crystals with weak electron–phonon coupling (S = 13) produce deep blue photoluminescence at RT. In contrast, due to the strong electron–phonon coupling with S = 181, $(C_7H_7N_2)_2PbCl_4$ exhibits an STE-derived broadband white emission at RT, which is almost the highest value among the bulk semiconductor materials we know so far.

The Huang–Rhys factor (S) is often employed to quantify the strength of electron–phonon coupling.[76] It has been reported that materials with self-trapping emission usually have large S, as shown in Table 2.

3.4. Temperature and pressure

External factors such as temperature and pressure can effectively adjust the structure and photoelectric properties of LDMHs. Perovskite materials usually undergo phase transition caused by the configurational changes of organic cation when the temperature changes,[92,93] which further affect the

photoelectric properties. For example, as the temperature increases, the organic cation arrangement becomes disordered, and the point of disorder is called the melting temperature[11] (Fig. 12(a)). The disordered arrangement of organic cations results in abrupt changes in the lattice parameters along the organic direction and changes in the spacing of 2D layered structures. Aurang Zeb et al.[94] reported an organic–inorganic hybrid 1D perovskite crystal has an obvious phase transformation at about T_c = 202 K and remarkable change of dielectric response (Fig. 12(b)), which is caused by the ordered–disordered transition of organic cations. It proves that the crystal lattice-related phase transition is related to the conformation of the alkylammonium chain.

Abid et al.[95] reported a single-structure phase transition of $(C_9H_{19}NH_3)_2PbI_2Br_2$ below RT with changes in the conformation alkylammonium chains, which is attributed to the reduced conformational disorder of the methylene units of the alkyl chains. In addition, the detailed investigation of the Raman spectra of $(C_9H_{19}NH_3)_2PbI_2Br_2$ at different temperatures is researched, and a mutation of the methylene C–H stretching frequency is found. As the test temperature approaches the transition temperature (230 K), a sharp drop in the change in crystallographic parameters occurs. This reduction results in a shift in the peak positions corresponding to symmetric and antisymmetric C–H stretching to lower frequencies, accompanied by a decrease in the peak intensity accompanying C–H stretching (Fig. 12(c)).

Furthermore, temperature also has a great influence on the STE emission. The STE emissions of some 2D 100-oriented perovskite can only be observed at low temperature (Fig. 12(d)).[18,50c,96] For example, Chen et al.[75] reported that
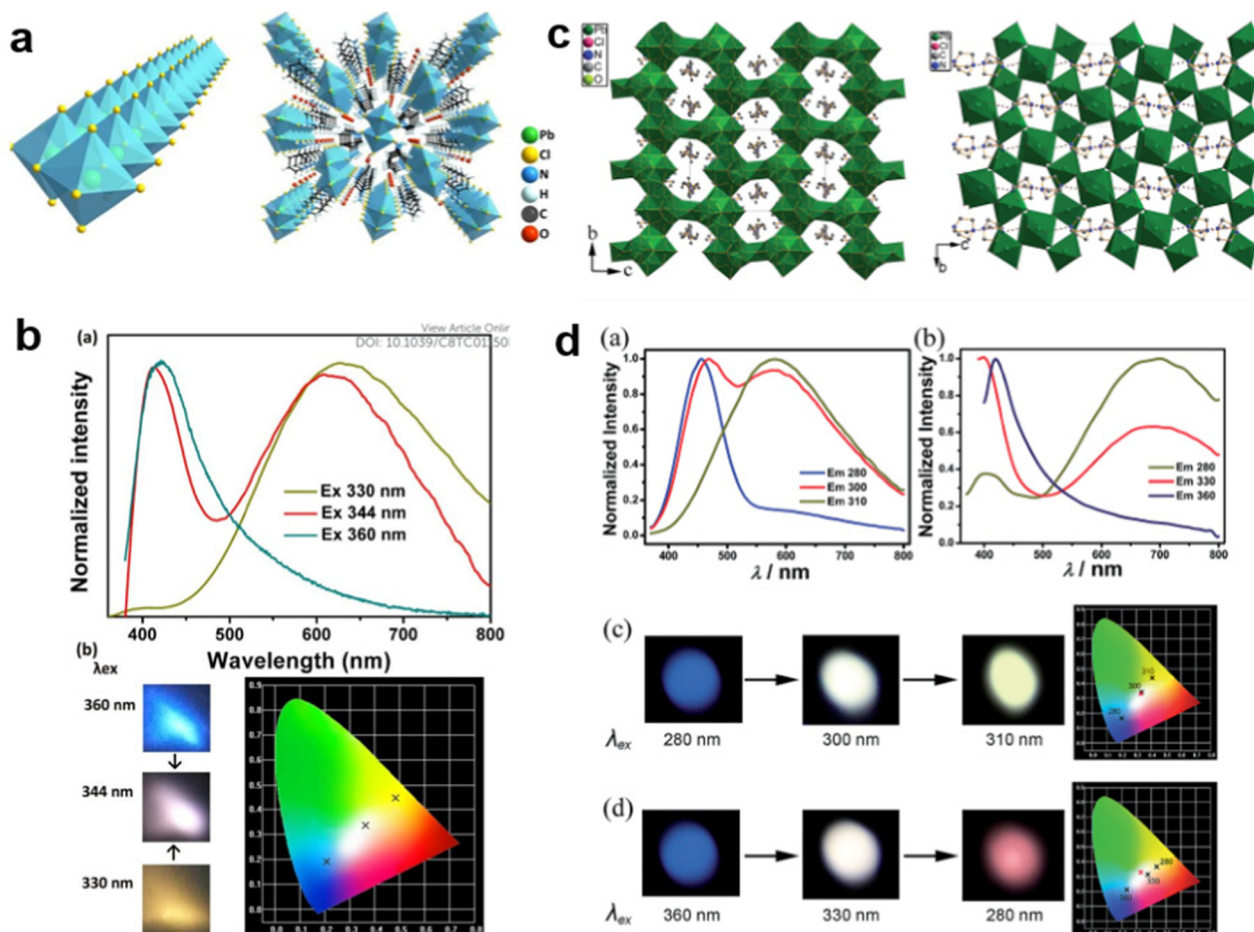
Fig. 9 (a) The structure of 1D hybrid perovskite $C_5H_{14}N_2PbCl_4 \cdot H_2O$.[65] (b) Emission spectra and photoluminescence photographs corresponding CIE chromaticity coordinates of $C_5H_{14}N_2PbCl_4 \cdot H_2O$ excited by different energies. Reprinted with permission.[65] Copyright 2013 The Royal Society of Chemistry. (c) The structures of hybrid perovskites $(H_2DABCO)(Pb_2Cl_6)$ and $(H_3O)(Et_2-DABCO)_8(Pb_{21}Cl_{59})$.[66] (d) Emission spectra and photoluminescence photographs corresponding CIE chromaticity coordinates of $(H_2DABCO)(Pb_2Cl_6)$ and $(H_3O)(Et_2-DABCO)_8(Pb_{21}Cl_{59})$ excited by different energies. Reprinted with permission.[66] Copyright 2015 The Royal Society of Chemistry.

the STE emission of 2D $(C_7H_7N_2)_2PbBr_4$ appeared at approximately 230 K and prevailed with decreasing temperature (Fig. 12(e)). The mechanism is shown in Fig. 12(f); when temperatures are relatively high, the STEs are easily detrapped from the STE states to FE states, and the detrapping process will be suppressed when the temperature is low.[18] Therefore, STEs emission gradually appears and increases with decreasing temperature.

Recently, pressure-induced emission (PIE) has been found in some LDMHs;[97] the emission intensity increased significantly upon compression by pressure, such as 1D $EAPbI_3$[24] (Fig. 13(a)) and 2D $(PEA)_2PbBr_4$[26] (Fig. 13(b)). Moreover, the pressure effect can also regulate the structure distortion of $(BA)_4AgBiBr_8$ to achieve self-trapped exciton emission.[27] As shown in Fig. 13(c), the luminescence of $(BA)_4AgBiBr_8$ was enhanced with increasing pressure. Zou et al.[25] reported the PIE in 1D $C_4N_2H_{14}SnBr_4$. The pressure-dependent PL intensity of $C_4N_2H_{14}SnBr_4$ was recorded (Fig. 13(d)), and the mechanism is shown in Fig. 13(e). Under atmospheric conditions, the self-trapped excitons are easy to detrap and return to free exciton

states; therefore, there is no photoluminescence. With the increase in the pressure, the degree of $[SnBr_6]^{4-}$ octahedral distortion increases, leading to the enhancement of the self-trapped states, which increases the energy of the excitons to detrap. Thus, the self-trapping emission is greatly enhanced.

3.5. Doping metal ions to enhance luminescence

Doping metals would be an effective strategy to tune the luminescence performance and improve the PLQE of LDMHs.[98] For example, extensive research on Mn^{2+} doping has been carried out due to exciton energy transition between from the FEs to the Mn^{2+} d-states and the internal transition of Mn^{2+} ions from $^4T_1$ to $^6A_1$; thus, a low-energy emission peak at about 600 nm was produced.[99] Cheng et al. grew a centimeter-size 2D layered $(CH_3NH_3)_2MnCl_4$ single crystal (Fig. 14(a)) and illustrated the temperature-dependent PL spectra (Fig. 14(b)).[100] Obviously, the PL intensity of $(CH_3NH_3)_2MnCl_4$ increases with decreasing temperature. The efficient emission was obtained thanks to the electronic transition $(t_{2g})^3(e_g)^2-(t_{2g})^4(e_g)^1$ of the Mn^{2+} ions (Fig. 14(c)).
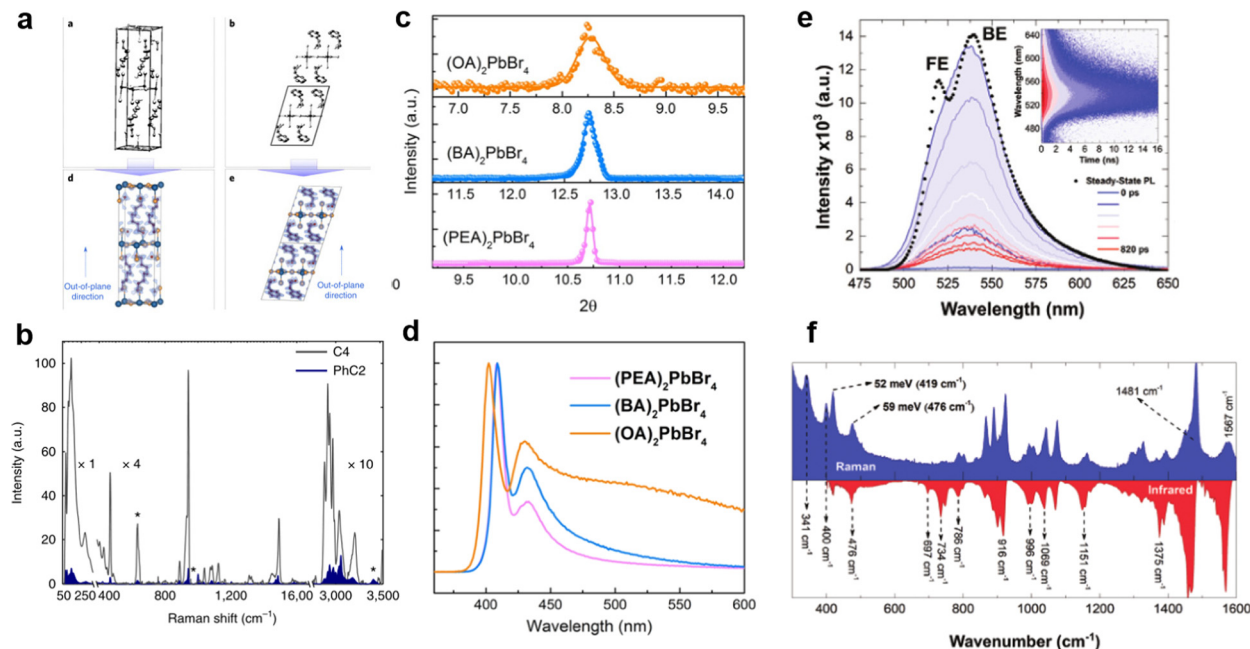
Fig. 10 (a) The structure of 2D perovskites BA_2PbBr_4 and PEA_2PbBr_4.[23] (b) Raman spectrum of BA_2PbBr_4 and PEA_2PbBr_4. Reprinted with permission.[23] Copyright 2018 Springer Nature. (c) XRD spectra in the (004) planes of the single crystals with different organic cations.[72] (d) PL spectra of the single crystals with different organic cations. Reprinted with permission.[72] Copyright 2020 American Chemical Society. (e) The time-resolved PL spectra reconstruction at different times.[69] (f) Raman and attenuated total reflectance infrared spectra. Reprinted with permission.[69] Copyright 2020 Wiley-VCH.
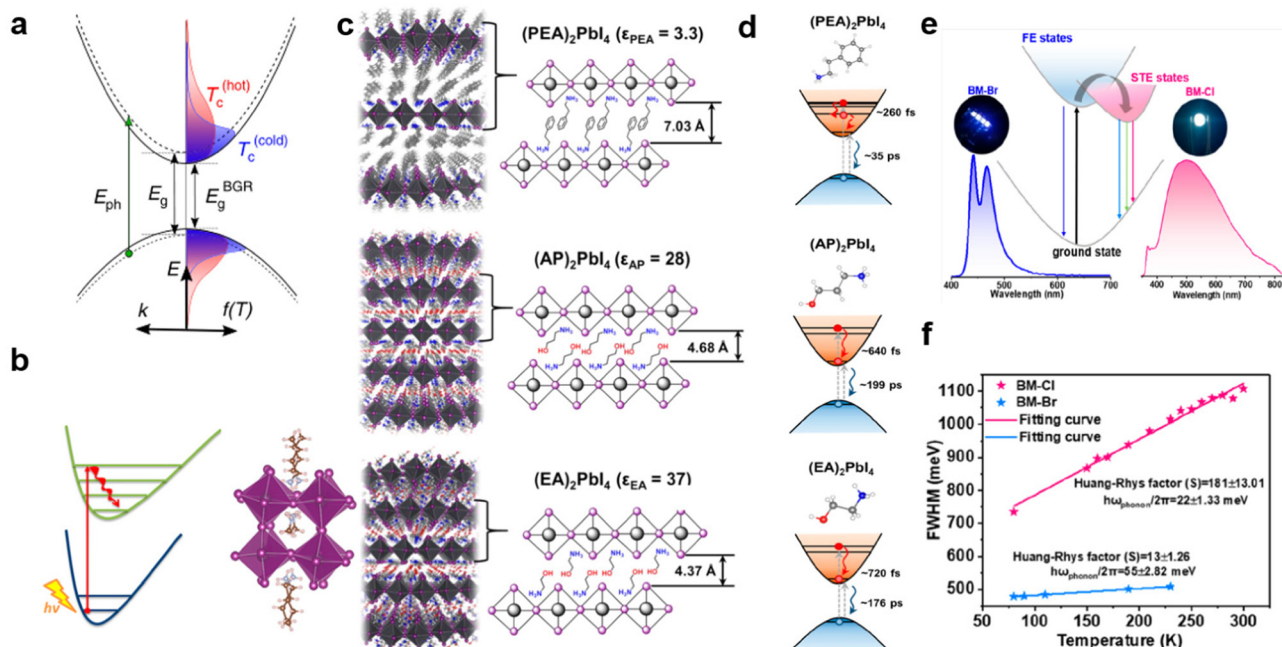

Fig. 11 (a) The schematic representation showing the carrier cooling process. Reprinted with permission.[70c] Copyright 2015 Springer Nature. (b) The faster hot-carrier decay rate in 2D $(BA)_2(MA)Pb_2I_7$. Reprinted with permission.[73] Copyright 2018 American Chemical Society. (c) Schematic illustrations of $(PEA)_2PbI_4$, $(AP)_2PbI_4$, and $(EA)_2PbI_4$ single crystals. (d) Hot electron relaxation and electron–hole pair recombination processes after high-energy excitation. Reprinted with permission.[74] Copyright 2018 American Chemical Society. (e) Absorption and emission spectra for the bulk $(C_7H_7N_2)_2PbBr_4$ and $(C_7H_7N_2)_2PbCl_4$ crystals at RT. (f) The FWHM of the broadband emission peak vs. temperature was plotted to obtain the Huang–Rhys factor S. Reprinted with permission.[75] Copyright 2022 American Chemical Society.

Table 2 Huang–Rhys factor (S) of reported semiconductor materials

Compounds	Huang–Rhys factor (S)
$(C_7H_7N_2)_2PbCl_4$[75]	181
$(C_7H_7N_2)_2PbBr_4$[75]	13
Cs_4SnBr_6[42]	107
$(NMEDA)PbBr_4$[42]	82
$Cs_2NaInCl_6$[77]	80
$Cs_3Bi_2I_9$[78]	79.5
$C_4N_2H_{14}PbBr_4$[42]	57
$Rb_3Sb_2I_9$[78]	50.4
$Cs_3Sb_2I_9$[78]	42.7
$Cs_2AgInCl_6$[79]	41
$Cs_2AgBiBr_6$[80]	11.9
$MAPbI_3$[81]	5–20
$CsPbBr_3$[82]	0.55
$CsPbX_3$, X = Br, Cl, I[83]	0.075–0.247
$(PEA)_2PbI_4$[84]	0.44–2.49
$(BA)_2(MA)_{n-1}PbnI_{3n+1}$[85]	1.24
$NaCl$[86]	42
$AgCl/Br$[87]	22
$MgCl_2$[88]	4
$MnCl_2$[88]	2.4
$CdCl_2$[88]	4.5
$CdSe$[89]	1
$ZnSe$[90]	0.3
Cs_2NaYCl_6[91]	6.86
K_2NaScF_6[91]	3.50
K_2NaGaF_6[91]	3.12

Zhou et al.[28] reported an Mn^{2+}-doped 1D $C_4N_2H_{14}PbBr_4$ with bright white emission, and the PL spectra and the images (inset) of the series of Mn-doped $C_4N_2H_{14}PbBr_4$ upon UV excitation are shown in Fig. 14(d). Dual emission at ∼390 and ∼485 nm recorded for pristine $C_4N_2H_{14}PbBr_4$ originates from FEs and STEs states. Eventually, efficient white emissions were obtained in Mn^{2+}-doped 1D $C_4N_2H_{14}PbBr_4$ by combining the broadband blue emission of STEs and red emission originating from the d–d transition of Mn^{2+}.[101] The CIE coordinates of the Mn^{2+}-doped $C_4N_2H_{14}PbBr_4$ was displayed in Fig. 14(e), and the CRI and PLQE of Mn^{2+}-doped $C_4N_2H_{14}PbBr_4$ were increased to 87 and 28%, respectively. In the Mn^{2+}-doped $C_4N_2H_{14}PbBr_4$, the blue emission at ∼485 nm remains relatively unchanged, but the near-UV emission is obviously quenched at 390 nm and an additional broadband emission appeared at 605 nm due to ligand field transition ($^4T_1$ to $^6A_1$) of Mn^{2+} (Fig. 14(f)).[102] Dutta et al. synthesized a layered Mn^{2+}-doped L_2PbX_4 (X = Cl, Br, I) single crystal using a solution-phase colloidal approach (Fig. 14(g)).[103] Mn^{2+}-doped L_2PbX_4 presents additional dopant emission at about 600 nm, when the intrinsic emission located at 420 nm (Fig. 14(h)). Moreover, doping Mn^{2+} facilitates exciton energy transition and achieves satisfactory PLQE of ∼61%. Fig. 14(i) indicates the stability in retaining intense emission of Mn^{2+}-doped L_2PbX_4 microcrystals under ambient conditions.

In addition to doping Mn^{2+}, other doping metals elements in LDMHs have been investigated to improve the luminescence efficiency and avoid the proportion of toxic lead, such as Sn^{3+},[31,104] Sb^{2+},[98a,98b] Bi^{3+},[105] Fe^{3+},[106] In^+,[107] Na^+,[108] Ag^+,[109]
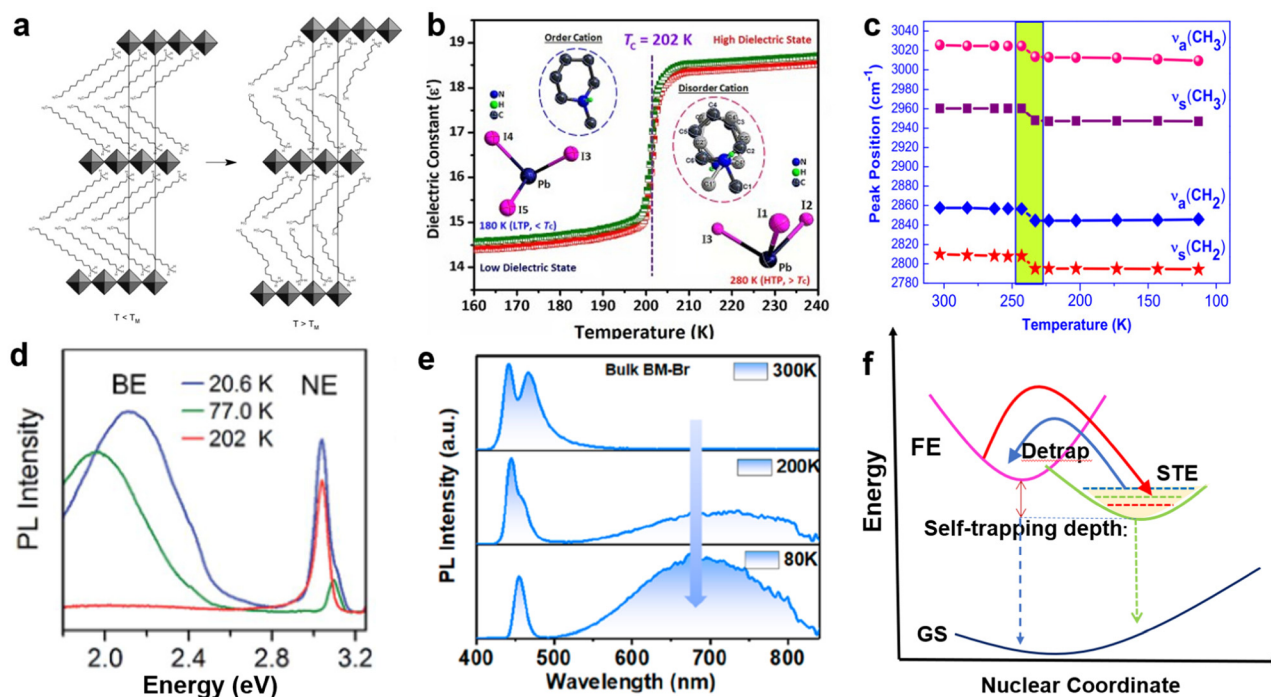

Fig. 12 (a) Schematic depiction of the melting transition in $(C_nH_{2n+1}NH_3)_2PbI_4$ compounds. Reproduced with permission.[11] 2019 American Chemical Society. (b) Phase transition and dielectric response of 1D perovskite structural phase transition induced by temperature. Reproduced with permission.[94] Copyright 2018 The Royal Society of Chemistry. (c) Peak position of the methylene C–H stretching at different temperatures between 303 K and 113 K. Reproduced with permission.[95] (d) The broadband emission appears at low temperature in 100-oriented 2D perovskite. Reproduced with permission.[50c] Copyright 2017 The Royal Society of Chemistry. (e) Temperature-dependent emission spectra for bulk $(C_7H_7N_2)_2PbBr_4$ crystals. Reproduced with permission.[75] Copyright 2022 American Chemical Society. (f) Graphs of low-dimensional perovskite excitons self-trapping and detrapping process.
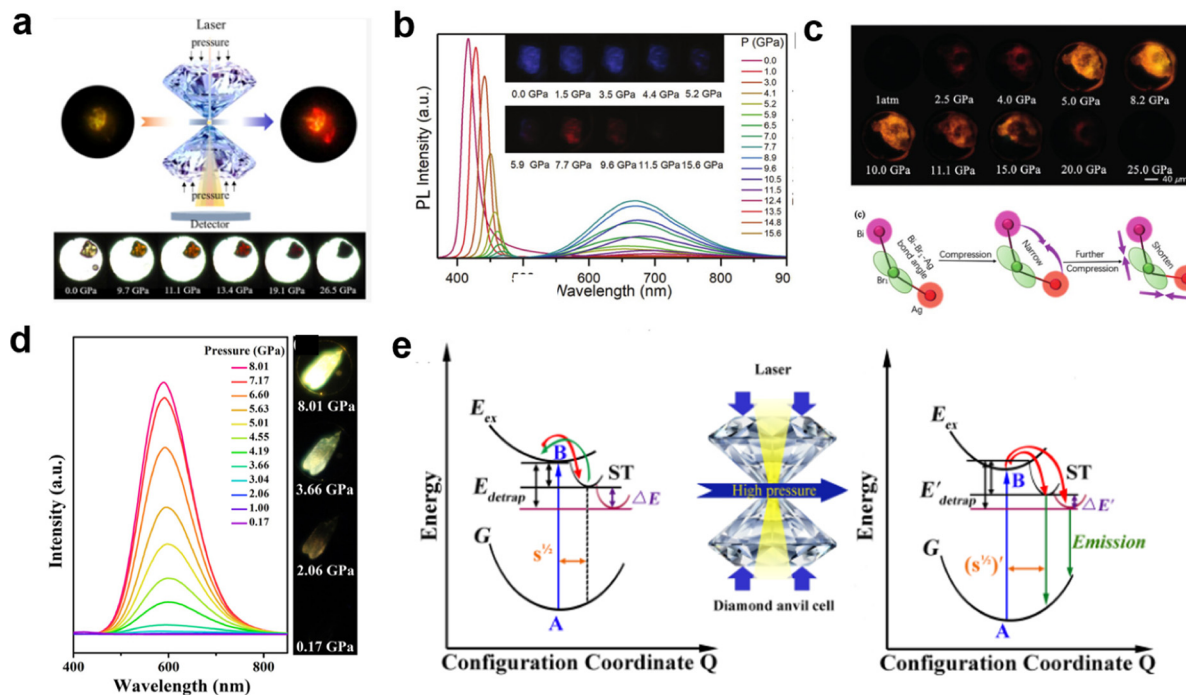
Fig. 13 (a) Schematic diagram of 1D EAPbI$_3$ luminescence intensity increasing with pressure. Reproduced with permission.[24] 2020 American Chemical Society. (b) PL spectra of (PEA)$_2$PbBr$_4$ as a function of pressure and PL micrographs upon compression. Reproduced with permission.[26] 2019 Wiley-VCH Verlag GmbH. (c) The photomicrograph shows the enhanced emission of (BA)$_4$AgBiBr$_8$ with increasing pressure. Reprinted with permission.[27] Copyright 2019 Wiley-VCH. (d) Pressure-dependence of the PL spectra of C$_4$N$_2$H$_{14}$SnBr$_4$. (e) Schematic diagram of the pressure-induced emission mechanism of self-trapped exciton. Reproduced with permission.[25] Copyright 2019 American Chemical Society.

and multicomponent metal.[110] Fig. 15(a) and (b) show the fabricated image and crystal structure of 0D (C$_8$NH$_{12}$)$_4$Bi$_{0.57}$-Sb$_{0.43}$Br$_7$·H$_2$O single crystal by Zhang *et al.*,[30] and the ratio of Pb and Sb (0.59 : 0.41) in single crystals was estimated by energy dispersive spectroscopy (EDS), as depicted in Fig. 15(e). Moreover, compared to (C$_8$NH$_{12}$)$_4$BiBr$_7$·H$_2$O and the reported 0D Sn-based perovskites,[104] different PL properties were reported in (C$_8$NH$_{12}$)$_4$Bi$_{0.57}$Sb$_{0.43}$Br$_7$·H$_2$O. The super broadband emission with 400 to 850 nm was exhibited in Fig. 15(c), and the PLQE increases from 0.7% to 4.5%. The TA spectra confirmed the STEs (Fig. 15(d)). As shown in Fig. 15(f), the mechanism of super broadband emission was attributed to the synergistic effect of FEs and STEs in the [BiBr$_6$]$^{3-}$ and [SbBr$_6$]$^{3-}$ species. The FEs are captured by the intrinsic STEs state, followed by energy transfer to the newly generated STEs state caused by the addition of the [SbBr$_6$]$^{3-}$ species.[111] Finally, the PLQE of super broadband emission was significantly enhanced due to the singlet and triplet STEs.[112] Wei *et al.* reported a series of 0D In–Sb doped BAPPIn$_{2-2x}$Sb$_{2x}$Cl$_{10}$ (BAPP = C$_{10}$H$_{28}$N$_4$, x = 0–1) perovskite single crystals with adjustable emission.[107] As shown in Fig. 15(g), a series of BAPPIn$_{2-2x}$Sb$_{2x}$Cl$_{10}$ single crystals show different colored emission under irradiation condition of UV light (λ_{ex} = 365 nm) with different doped contents of Sb. Interestingly, with the addition of Sb, there are obvious blue and yellow double emission bands ($\sim$440 and $\sim$560 nm) in the PL spectrum. Moreover, a series of BAPPIn$_{2-2x}$Sb$_{2x}$Cl$_{10}$ materials were used in the field of

anti-counterfeiting due to their excellent properties, such as afterglow emission, as well as high spatial and temporal resolution. Fig. 15(h) displays a 2020-shaped module-filled BAPPIn$_{1.996}$Sb$_{0.004}$Cl$_{10}$ powders, which displays a misleading profile with 8888-shaped under visible light and changes to a yellow-white emission with 2020-shaped under condition of 254 and 365 nm, respectively. The organic emission of BAPPSb$_2$Cl$_{10}$ was almost quenched, which may be due to the energy transfer of the organic cation widely present in the doped system to the Sb^{3+} emission center. In this case, the two launch centers operate independently, providing a perfect complement of colors, namely, blue and yellow emission, which eventually appear as a bright white emission (Fig. 15(i)). The WLED device and CIE coordinates of the emissions are depicted in Fig. 15(j), and distinguishable fluorescence colors of the as-fabricated flexible BAPPIn$_{1.996}$Sb$_{0.004}$Cl$_{10}$-PDMS (polydimethylsiloxane) are seen at 365 and 254 nm UV light (Fig. 15(k)).

Yu *et al.*[31] reported Sn-doped 2D PEA$_2$PbI$_4$ (PEA = phenyl-ethylammonium) crystal (Fig. 16(a)), which produces broadband emission with red-to-near-infrared thanks to the stronger exciton–phonon coupling, and the PLQE is significantly increased from 0.7% to 6.0%. PEA$_2$PbI$_4$ and doped 0.36%-Sn PEA$_2$PbI$_4$ generate green emission at 525 nm and bright broadband emission with red-to-near-infrared at the center of 710 nm (Fig. 16(b)). The emissions of PEA$_2$PbI$_4$ and Sn-doped PEA$_2$PbI$_4$ depend on exciton dynamics confined to the inorganic layer (Fig. 16(c)) and the relaxation channels of carriers in the excited
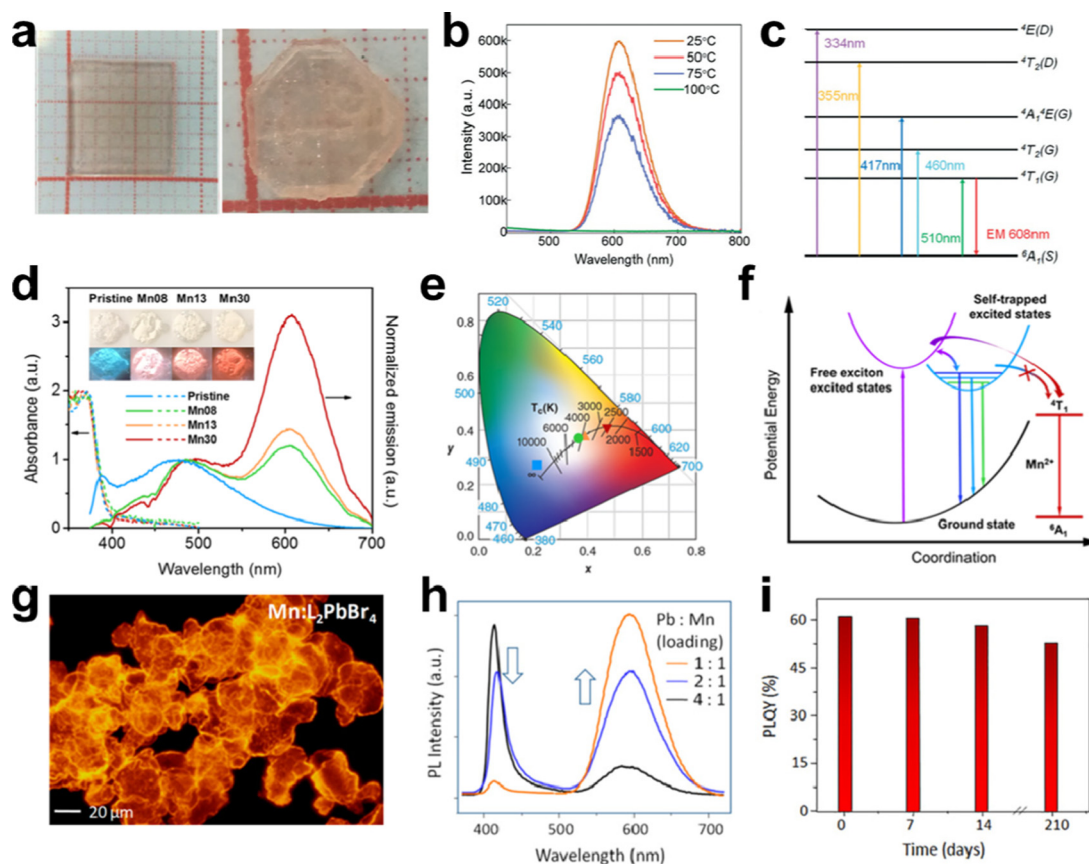
Fig. 14 (a) Photographs of layered $(CH_3NH_3)_2MnCl_4$ single crystals; (b) temperature-dependent luminescence spectra of $(CH_3NH_3)_2MnCl_4$ single crystals; (c) schematic diagram showing the energy absorption and emission processes of $(CH_3NH_3)_2MnCl_4$; reproduced with permission.[100] Copyright 2019 The Royal Society of Chemistry. (d) Absorption and emission spectra of the pristine and Mn-doped 1D $C_4N_2H_{14}PbBr_4$, the inset shows the images of the pristine and Mn-doped $C_4N_2H_{14}PbBr_4$ under ambient light (top) and UV light (365 nm, bottom); (e) CIE coordinates of the emissions of the pristine and Mn-doped $C_4N_2H_{14}PbBr_4$ upon UV excitation; (f) proposed energy diagram and excited state dynamics of Mn-doped 1D $C_4N_2H_{14}PbBr_4$; reproduced with permission.[28] Copyright 2017 American Chemical Society. (g) Optical microscopic images of Mn-doped L_2PbBr_4 microcrystals under UV irradiation; (h) PL spectra of Mn-doped L_2PbBr_4; (i) PLQE stability of Mn-doped L_2PbBr_4 microcrystals; reproduced with permission.[103] Copyright 2019 American Chemical Society.

perovskite (Fig. 16(d)). Zhang *et al.* synthesized two 2D $(PEA)_4$-$NaInCl_8$:Sb and $(PEA)_2CsNaInCl_7$:Sb single crystals by doping Sb.[108] The STEs captured in the introduced $[SbCl_6]^{3-}$ octahedron produced bright broadband emission with PLQE of 48.7%. The main dynamic process of initial and Sb-doped $(PEA)_4NaInCl_8$ is depicted in Fig. 16(e); the doped $[SbCl_6]^{3-}$ octahedron offers a new exciton capturing center and forms a Jahn–Teller-like distortion under the condition of excited state. The PL intensity of $(PEA)_4NaInCl_8$:Sb increased first and then decreased with the increase in the Sb content, and the optimal doping ratio is 2.13% (Fig. 16(f)).

In summary, both the internal components and external factors can modulate the STE emission of LDMHs. For internal components, choosing the large organic cations with polyamine groups or long chain amine can distort the inorganic skeleton, thus favoring exciton self-trapping. Passing from I, Br, to Cl, it tends to form STE broadband emission. In addition, the LDMHs with strong electron–phonon coupling (large S) generally produce STE emission. For the external factors, STE emission can be induced by proper pressure, and decreasing the

temperature can inhibit exciton detrapping and enhance STE emission. Furthermore, doping metal ions is also an effective way to modulate the STE emission and improve the PLQE of LDMHs, such as doping Mn^{2+} and Sn^{2+}.

4. Prospects and outlook

(1) Solid-state lighting is emerging in the automotive, architectural, and general lighting markets over the last decade. Despite significant progress in white light-emitting diodes (WLED), there are still many problems and challenges that limit its development, for example, single color rendering is usually poor due to the discontinuity of the emission spectrum. On the other hand, mixing phosphors will decrease in efficiency due to the self-absorption effect. At the same time, the luminous color of phosphors varies with time due to different attenuation degrees. To solve these problems, an ideal solution is to develop a single component of broadband spectrum white phosphor powder excited by ultraviolet light. At present, this
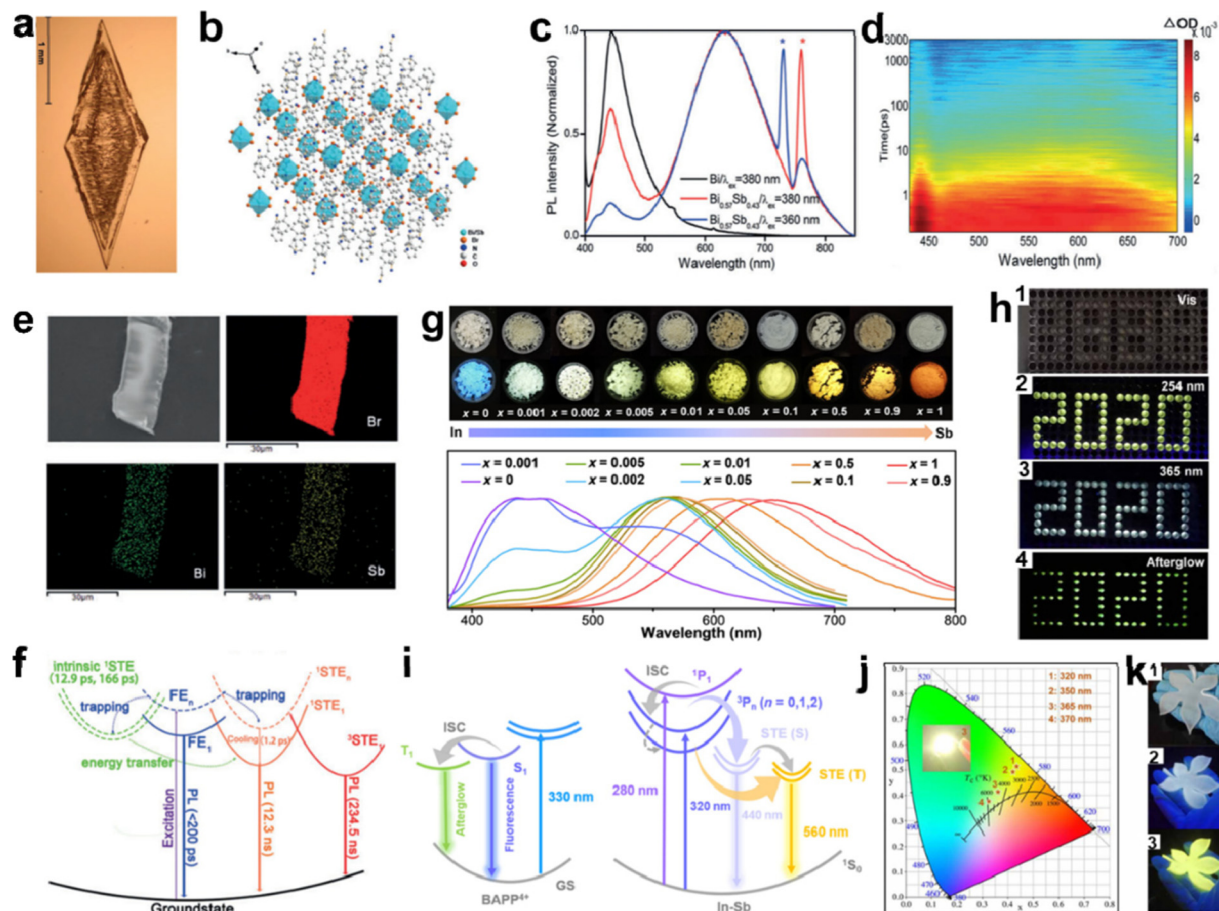
Fig. 15 (a) and (b) Image and structure diagram of the $(C_8NH_{12})_4Bi_{0.57}Sb_{0.43}Br_7 \cdot H_2O$ single crystal; (c) room temperature PL spectra of $(C_8NH_{12})_4BiBr_7 \cdot H_2O$ and $(C_8NH_{12})_4Bi_{0.57}Sb_{0.43}Br_7 \cdot H_2O$; (d) contour plot of the fs TA spectrum upon photoexcitation at 320 nm, (e) EDS elemental mapping of Br, Bi, and Sb elements; (f) schematic energy level diagram of $(C_8NH_{12})_4Bi_{0.57}Sb_{0.43}Br_7 \cdot H_2O$ single crystal; reproduced with permission.[30] Copyright 2019 Wiley-VCH. (g) Images and PL spectra under visible and UV light of a batch of $BAPPIn_{2-2x}Sb_{2x}Cl_{10}$; (h) photos of patterned single $BAPPIn_{1.996}Sb_{0.004}Cl_{10}$ crystals under the excitation of (1) visible light, (2) 254 nm UV light, (3) 365 nm UV light on, and (4) 365 nm UV light off (afterglow); (i) schematic illustration of the photophysical processes in $BAPPIn_{2-2x}Sb_{2x}Cl_{10}$; (j) excitation wavelength-dependent CIE coordinate diagram of $BAPPIn_{1.996}Sb_{0.004}Cl_{10}$ (inset is the image of working WLED); (k) images of leaf-like shape $BAPPIn_{1.996}Sb_{0.004}Cl_{10}$-PDMS complex under (1) visible light, (2) 365 nm UV light, and (3) 254 nm UV light, respectively; reproduced with permission.[107] Copyright 2021 American Association for the Advancement of Science.

material is relatively rare. Most of them are inorganic materials doped with rare earth elements. The luminescence efficiency of these inorganic phosphors is generally low, and the manufacturing process is complex and the manufacturing cost is higher. For these reasons, it is very important to develop new types of white phosphor. The organic–inorganic hybrid LDMHs is a very promising illuminating material for WLED.

(2) Compared with 3D perovskites, the selection of organic cations for LDMHs is more abundant. We can not only regulate the structural dimension by selecting organic cations in large size but also rationally design organic cations to achieve the regulation of photoelectric properties. LDMHs exhibit excellent luminescence due to their quantum confined effect and large exciton binding energies. Also, by the rational design of organic cations, their emission type, fluorescence quantum efficiency, and so on can be regulated.

(3) In addition, LDMHs are not limited to the application on LEDs. Their photoelectric response characteristics make them

promising materials for photodetectors, lasers, biosensors, and ferroelectric response devices. Multifunctional LDMHs with abundant dimensions and structures are looking forward to the potential applications.

Overcoming

(1) However, the origin of the broadband emission in LDMHs is still hotly debated. Different mechanisms have recently been proposed to explain the origin of such emission. These contradicting explanations reported in the literature motivated us to decipher the source of broadband emission. Figuring out the luminescence mechanism will enable the development of synthesis strategies that fully control the broadband luminescence and defect properties.

(2) LDMHs has been widely used in LED devices due to its high exciton binding energy, but there is still a long way to go in
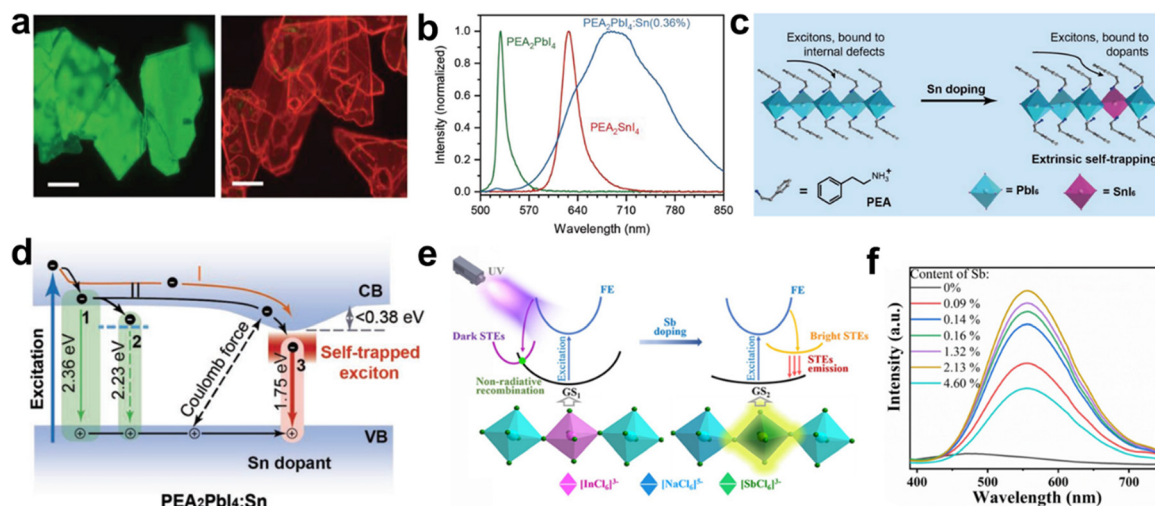
Fig. 16 (a) Fluorescence microscopy images of PEA_2PbI_4 and PEA_2PbI_4:Sn(0.36%) crystals. Scale bar: 100 μm; (b) microscopic PL spectra under $\lambda_{ex} =$ 470 nm; (c) schematic illustration of exciton trapping in pristine and Sn-doped 2D PEA_2PbI_4; (d) schematic illustration of radiative channels in Sn-doped PEA_2PbI_4. Arabic numerals 1, 2, and 3 represent the luminescence from free, bound excitons of pristine perovskite, and Sn-triggered STEs of Sn-doped perovskite, respectively; reproduced with permission.[31] Copyright 2018 Wiley-VCH. (e) Schematic energy level diagrams of $(PEA)_4NaInCl_8$ and $(PEA)_4NaInCl_8$:Sb; (f) PL spectra of $(PEA)_4NaInCl_8$:Sb with different Sb contents (Sb/In); reproduced with permission.[108] Copyright 2021 Wiley-VCH.

the development of phosphorescent materials and the technology of large-area LED devices. At present, LDMHs for red/green LED devices have been investigated by many researches, but there are still few reports on new material and luminescence mechanism in the development of blue LED. Moreover, device fabrication processes are still immature, including large-area LED and heterostructure devices.

(3) Although the stability of organic–inorganic hybrid perovskites has been greatly improved, the potential toxicity problem of Pb^{2+} has not been solved. Decrease environmental pollution is a key issue. At present, some people have tried to use other metal elements to replace or partially replace Pb to prepare lead-free or lead-less LDMHs. At present, it has been reported that Cu^{2+}, Mn^{2+}, Zn^{2+}, and other metal LDMHs show excellent luminescence characteristics; however, more mixing or doping metal LDMHs remain largely unexplored.

Author contributions

Y. Han and X. Cheng contributed equally to this work. All the authors contibuted to the discussion on the content, writing and editing for this menuscript prior to submission.

Conflicts of interest

The authors declare no competing interests.

Acknowledgements

References

1 (*a*) H. Lu, Y. Liu, P. Ahlawat, A. Mishra, W. R. Tress, F. T. Eickemeyer, Y. Yang, F. Fu, Z. Wang and C. E. Avalos, *Science*, 2020, 370; (*b*) X.-K. Liu, W. Xu, S. Bai, Y. Jin, J. Wang, R. H. Friend and F. Gao, *Nat. Mater.*, 2020, 1–12.

2 (*a*) H. Lin, C. Zhou, Y. Tian, T. Siegrist and B. Ma, *ACS Energy Lett.*, 2018, **3**, 54–62; (*b*) T. Zhu and X. Gong, *InfoMat*, 2021, **3**, 1039–1069.

3 Q. Yao, J. Zhang, K. Wang, L. Jing, X. Cheng, C. Shang, J. Ding, W. Zhang, H. Sun and T. Zhou, *J. Mater. Chem. C*, 2021, **9**, 7374–7383.

4 H. Lin, C. Zhou, Y. Tian, T. Siegrist and B. Ma, *ACS Energy Lett.*, 2017, **3**, 54–62.

5 H.-P. Wang, S. Li, X. Liu, Z. Shi, X. Fang and J.-H. He, *Adv. Mater.*, 2021, **33**, 2003309.

6 D. Yu, P. Wang, F. Cao, Y. Gu, J. Liu, Z. Han, B. Huang, Y. Zou, X. Xu and H. Zeng, *Nat. Commun.*, 2020, **11**, 3395.

7 K. Park, J. W. Lee, J. D. Kim, N. S. Han, D. M. Jang, S. Jeong, J. Park and J. K. Song, *J. Phys. Chem. Lett.*, 2016, **7**, 3703–3710.

8 G. Zhou, M. Li, J. Zhao, M. S. Molokeev and Z. Xia, *Adv. Opt. Mater.*, 2019, **7**, 1901335.

9 J. Zhang, X. Yang, H. Deng, K. Qiao, U. Farooq, M. Ishaq, F. Yi, H. Liu, J. Tang and H. Song, *Nano-Micro Lett.*, 2017, **9**, 36.

10 (*a*) N. Kawano, M. Koshimizu, G. Okada, Y. Fujimoto, N. Kawaguchi, T. Yanagida and K. Asai, *Sci. Rep.*, 2017, **7**, 1–8; (*b*) L. Zhou, J. F. Liao, Z. G. Huang, J. H. Wei, X. D. Wang, W. G. Li, H. Y. Chen, D. B. Kuang and C. Y. Su, *Angew. Chem., Int. Ed.*, 2019, **58**, 5277–5281; (*c*) B.-B. Cui, N. Yang, C. Shi, S. Yang, J.-Y. Shao, Y. Han, L. Zhang, Q. Zhang, Y.-W. Zhong and Q. Chen, *J. Mater. Chem. A*, 2018, **6**, 10057–10063;

(d) Z. Yuan, C. Zhou, Y. Tian, Y. Shu, J. Messier, J. C. Wang, L. J. van de Burgt, K. Kountouriotis, Y. Xin and E. Holt, *Nat. Commun.*, 2017, **8**, 14051.

11 L. Mao, C. C. Stoumpos and M. G. Kanatzidis, *J. Am. Chem. Soc.*, 2019, **141**, 1171–1190.

12 (a) L. Mao, Y. Wu, C. C. Stoumpos, M. R. Wasielewski and M. G. Kanatzidis, *J. Am. Chem. Soc.*, 2017, **139**, 5210–5215; (b) E. R. Dohner, E. T. Hoke and H. I. Karunadasa, *J. Am. Chem. Soc.*, 2014, **136**, 1718–1721; (c) E. R. Dohner, A. Jaffe, L. R. Bradshaw and H. I. Karunadasa, *J. Am. Chem. Soc.*, 2014, **136**, 13154–13157.

13 A. A. Zhumekenov, M. I. Saidaminov, O. F. Mohammed and O. M. Bakr, *Joule*, 2021, **5**, 2027.

14 C. M. Iaru, J. J. Geuchies, P. M. Koenraad, D. L. Vanmaekelbergh and A. Y. Silov, *ACS Nano*, 2017, **11**, 11024–11030.

15 D. Y. Park, S. J. An, C. Lee, D. A. Nguyen, K. N. Lee and M. S. Jeong, *J. Phys. Chem. Lett.*, 2019, **10**, 7942–7948.

16 Q. Zhang, Y. Ji, Z. Chen, D. Vella, X. Wang, Q. H. Xu, Y. Li and G. Eda, *J. Phys. Chem. Lett.*, 2019, **10**, 2869–2873.

17 (a) M. D. Smith, A. Jaffe, E. R. Dohner, A. M. Lindenberg and H. I. Karunadasa, *Chem. Sci.*, 2017, **8**, 4497–4504; (b) B. Febriansyah, T. Borzda, D. Cortecchia, S. Neutzner, G. Folpini, T. M. Koh, Y. Li, N. Mathews, A. Petrozza and J. England, *Angew. Chem., Int. Ed.*, 2020, **59**, 10791.

18 M. D. Smith, A. Jaffe, E. R. Dohner, A. M. Lindenberg and H. I. Karunadasa, *Chem. Sci.*, 2017, **8**, 4497–4504.

19 L. Mao, Y. Wu, C. C. Stoumpos, M. R. Wasielewski and M. G. Kanatzidis, *J. Am. Chem. Soc.*, 2017, **139**, 5210–5215.

20 C. Li, J. Yang, F. Su, J. Tan, Y. Luo and S. Ye, *Nat. Commun.*, 2020, **11**, 1–8.

21 (a) K. Wang, Y. Yuan, S. Du, Q. Yao, J. Zhang, C. Shang, C. Li, H. Sun, W. Zhang, J. Ding and T. Zhou, *J. Phys. Chem. C*, 2021, **125**, 15223–15232; (b) M. D. Smith, B. A. Connor and H. I. Karunadasa, *Chem. Rev.*, 2019, **119**, 3104–3139.

22 Y. Gao, E. Shi, S. Deng, S. B. Shiring, J. M. Snaider, C. Liang, B. Yuan, R. Song, S. M. Janke and A. Liebman-Peláez, *Nat. Chem.*, 2019, **11**, 1151–1157.

23 X. Gong, O. Voznyy, A. Jain, W. Liu, R. Sabatini, Z. Piontkowski, G. Walters, G. Bappi, S. Nokhrin and O. Bushuyev, *Nat. Mater.*, 2018, **17**, 550–556.

24 Y. Liang, Y. Zang, X. Huang, C. Tian, X. Wang and T. Cui, *J. Phys. Chem. C*, 2020, **124**, 8984–8991.

25 Y. Shi, Z. Ma, D. Zhao, Y. Chen and Y. Cao, *J. Am. Chem. Soc.*, 2019, **141**(16), 6504–6508.

26 L. Zhang, L. Wu, K. Wang and B. Zou, *Adv. Sci.*, 2019, **6**, 1801628.

27 Y. Fang, L. Zhang, L. Wu, J. Yan and B. Zou, *Angew. Chem., Int. Ed.*, 2019, **58**, 15249.

28 C. Zhou, Y. Tian, O. Khabou, M. Worku, Y. Zhou, J. Hurley, H. Lin and B. Ma, *ACS Appl. Mater. Interfaces*, 2017, **9**, 40446–40451.

29 Z. Li, Y. Li, P. Liang, T. Zhou, L. Wang and R.-J. Xie, *Chem. Mater.*, 2019, **31**, 9363–9371.

30 R. Zhang, X. Mao, Y. Yang, S. Yang, W. Zhao, T. Wumaier, D. Wei, W. Deng and K. Han, *Angew. Chem., Int. Ed.*, 2019, **58**, 2725–2729.

31 J. Yu, J. Kong, W. Hao, X. Guo, H. He, W. R. Leow, Z. Liu, P. Cai, G. Qian, S. Li, X. Chen and X. Chen, *Adv. Mater.*, 2019, **31**, e1806385.

32 (a) C. Zhou, H. Lin, Y. Tian, Z. Yuan, R. Clark, B. Chen, J. Neu, T. Besara, T. Siegrist, E. Lambers, P. Djurovich and B. Ma, *Chem. Sci.*, 2018, **9**, 586; (b) B.-B. Cui, Y. Han, B. Huang, Y. Zhao, X. Wu, L. Liu, G. Cao, Q. Du, N. Liu and W. Zou, *Nat. Commun.*, 2019, **10**, 1–8.

33 Z. Wu, C. Ji, Z. Sun, S. Wang, S. Zhao, W. Zhang, L. Li and J. Luo, *J. Mater. Chem. C*, 2018, **6**, 1171–1175.

34 L. Mao, Y. Wu, C. C. Stoumpos, B. Traore, C. Katan, J. Even, M. R. Wasielewski and M. G. Kanatzidis, *J. Am. Chem. Soc.*, 2017, **139**, 11956–11963.

35 (a) W. P. Wong, J. Yin, B. Chaudhary, X. Y. Chin, D. Cortecchia, S.-Z. A. Lo, A. C. Grimsdale, O. F. Mohammed, G. Lanzani and C. Soci, *ACS Mater. Lett.*, 2019, **2**, 20–27; (b) D. Ghosh, E. Welch, A. J. Neukirch, A. Zakhidov and S. Tretiak, *J. Phys. Chem. Lett.*, 2020, **11**, 3271–3286.

36 M. D. Smith and H. I. Karunadasa, *Acc. Chem. Res.*, 2018, **51**(3), 619–627.

37 C. Zhou, H. Lin, H. Shi, Y. Tian and B. Ma, *Angew. Chem., Int. Ed.*, 2017, 130.

38 J. Yin, H. Li, D. Cortecchia, C. Soci and J.-L. Brédas, *ACS Energy Lett.*, 2017, **2**, 417–423.

39 (a) P. Cai, Y. Huang and H. J. Seo, *J. Phys. Chem. Lett.*, 2019, **10**, 4095–4102; (b) A. Biswas, R. Bakthavatsalam, S. R. Shaikh, A. Shinde, A. Lohar, S. Jena, R. G. Gonnade and J. Kundu, *Chem. Mater.*, 2019, **31**, 2253–2257.

40 D. Cortecchia, S. Neutzner, A. R. Srimath Kandada, E. Mosconi, D. Meggiolaro, F. De Angelis, C. Soci and A. Petrozza, *J. Am. Chem. Soc.*, 2017, **139**, 39–42.

41 (a) L. Zhou, J. F. Liao, Z. G. Huang, J. H. Wei, X. D. Wang, H. Y. Chen and D. B. Kuang, *Angew. Chem., Int. Ed.*, 2019, **131**, 15581–15586; (b) D. Han, H. Shi, W. Ming, C. Zhou, B. Ma, B. Saparov, Y.-Z. Ma, S. Chen and M.-H. Du, *J. Mater. Chem. C*, 2018, **6**, 6398–6405.

42 X. Wang, W. Meng, W. Liao, J. Wang, R.-G. Xiong and Y. Yan, *J. Phys. Chem. Lett.*, 2019, **10**, 501–506.

43 S. Kahmann, E. K. Tekelenburg, H. Duim, M. E. Kamminga and M. A. Loi, *Nat. Commun.*, 2020, **11**, 1–8.

44 J. Yin, R. Naphade, L. Gutiérrez Arzaluz, J.-L. Bredas, O. M. Bakr and O. F. Mohammed, *ACS Energy Lett.*, 2020, **5**(7), 2149–2155.

45 A. Wang, Y. Guo, Z. Zhou, X. Niu, Y. Wang, F. Muhammad, H. Li, T. Zhang, J. Wang, S. Nie and Z. Deng, *Chem. Sci.*, 2019, **10**, 4573.

46 B. Dhanabalan, R. D. Pothuraju, S. Marras, L. Pasquale, L. Manna, R. Krahne and M. P. Arciniegas, *Adv. Photon. Res.*, 2021, **2**, 2100005.

47 (a) Z. Yuan, C. Zhou, Y. Tian, Y. Shu, J. Messier, J. C. Wang, L. J. Van De Burgt, K. Kountouriotis, Y. Xin and E. Holt, *Nat. Commun.*, 2017, **8**, 14051; (b) R. Gautier, F. Massuyeau, G. Galnon and M. Paris, *Adv. Mater.*, 2019, **31**, 1807383.

48 C. Zhou, H. Lin, Y. Tian, Z. Yuan, R. Clark, B. Chen, L. J. van de Burgt, J. C. Wang, Y. Zhou and K. Hanson, *Chem. Sci.*, 2018, **9**, 586–593.

49 S. Wang, Y. Yao, J. Kong, S. Zhao, Z. Sun, Z. Wu, L. Li and J. Luo, *Chem. Commun.*, 2018, **54**, 4053–4056.

50 (a) I. Neogi, A. Bruno, D. Bahulayan, T. W. Goh, B. Ghosh, R. Ganguly, D. Cortecchia, T. C. Sum, C. Soci and N. Mathews, *ChemSusChem*, 2017, **10**, 3765–3772; (b) H. Hu, S. A. Morris, X. Qiao, D. Zhao, T. Salim, B. Chen, E. E. Chia and Y. M. Lam, *J. Mater. Chem. C*, 2018, **6**, 10301–10307; (c) M. D. Smith, A. Jaffe, E. R. Dohner, A. M. Lindenberg and H. I. Karunadasa, *Chem. Sci.*, 2017, **8**, 4497–4504.

51 B. Febriansyah, T. Borzda, D. Cortecchia, S. Neutzner, G. Folpini, T. M. Koh, Y. Li, N. Mathews, A. Petrozza and J. England, *Angew. Chem., Int. Ed.*, 2020, **59**, 10791–10796.

52 S. Wang, Y. Yao, Z. Wu, Y. Peng, L. Li and J. Luo, *J. Mater. Chem. C*, 2018, **6**, 12267–12272.

53 L. Mao, Y. Wu, C. C. Stoumpos, B. Traore, C. Katan, J. Even, M. R. Wasielewski and M. G. Kanatzidis, *J. Am. Chem. Soc.*, 2017, **139**, 5210–5215.

54 A. Yangui, S. Pillet, A. Lusson, E. E. Bendeif, S. Triki, Y. Abid and K. Boukheddaden, *J. Alloys Compd.*, 2017, **699**, 1122–1133.

55 D. Cortecchia, J. Yin, A. Petrozza and C. Soci, *J. Mater. Chem. C*, 2019, **7**, 4956–4969.

56 Y. Y. Pan, Y. H. Su, C. H. Hsu, L. W. Huang and C. C. Kaun, *Comput. Mater. Sci.*, 2016, **117**, 573–578.

57 A. Lemmerer and D. G. Billing, *CrystEngComm*, 2012, **14**, 1954–1966.

58 Y. Han, Y. Li, Y. Wang, G. Cao, S. Yue, L. Zhang, B. B. Cui and Q. Chen, *Adv. Opt. Mater.*, 2020, **8**, 1902051.

59 M. E. Kamminga, H. H. Fang, M. R. Filip, F. Giustino, J. Baas, G. R. Blake, M. A. Loi and T. T. M. Palstra, *Chem. Mater.*, 2016, **28**(13), 4554–4562.

60 L. L. Mao, P. J. Guo, M. Kepenekian, I. Hadar, C. Katan., J. Even, R. D. Schaller, C. C. Stoumpos and M. K. Kanatzidis, *J. Am. Chem. Soc.*, 2018, **140**(40), 13078–13088.

61 M. Zhang, L. Zhao, J. Xie, Q. Zhang, X. Wang, N. Yaqoob, Z. Yin, P. Kaghazchi, H. Li and C. Zhang, *Nat. Commun.*, 2021, **12**, 1–7.

62 S. Krishnamurthy, R. Naphade, W. J. Mir, S. Gosavi, S. Chakraborty, R. Vaidhyanathan and S. Ogale, *Adv. Opt. Mater.*, 2018, **6**, 1800751.

63 A. Yangui, D. Garrot, J.-S. Lauret, A. Lusson, G. Bouchez, E. Deleporte, S. Pillet, E.-E. Bendeif, M. Castro and S. Triki, *J. Phys. Chem. C*, 2015, **119**, 23638–23647.

64 T. Dammak and Y. Abid, *Opt. Mater.*, 2017, **66**, 302–307.

65 Y. Peng, Y. Yao, L. Li, Z. Wu, S. Wang and J. Luo, *J. Mater. Chem. C*, 2018, **6**, 6033–6037.

66 G.-E. Wang, G. Xu, M.-S. Wang, L.-Z. Cai, W.-H. Li and G.-C. Guo, *Chem. Sci.*, 2015, **6**, 7222–7226.

67 (a) B. Dhanabalan, Y. C. Leng, G. Biffi, M. L. Lin, P. H. Tan, I. Infante, L. Manna, M. P. Arciniegas and R. Krahne, *ACS Nano*, 2020, **14**, 4689–4697; (b) D. B. Straus, S. Hurtado Parra, N. Iotov, J. Gebhardt, A. M. Rappe, J. E. Subotnik, J. M. Kikkawa and C. R. Kagan, *J. Am. Chem. Soc.*, 2016, **138**, 13798–13801; (c) F. Thouin, D. A. Valverde-Chavez, C. Quarti, D. Cortecchia, I. Bargigia, D. Beljonne, A. Petrozza, C. Silva and A. R. Srimath Kandada, *Nat. Mater.*, 2019, **18**, 349–356.

68 (a) C. M. Iaru, J. J. Geuchies, P. M. Koenraad, D. Vanmaekelbergh and A. Y. Silov, *ACS Nano*, 2017, **11**, 11024–11030; (b) A. D. Wright, C. Verdi, R. L. Milot, G. E. Eperon, M. A. Perez-Osorio, H. J. Snaith, F. Giustino, M. B. Johnston and L. M. Herz, *Nat. Commun.*, 2016, 7.

69 R. F. Moral, J. C. Germino, L. G. Bonato, D. B. Almeida, E. M. Therézio, T. D. Atvars, S. D. Stranks, R. A. Nome and A. F. Nogueira, *Adv. Opt. Mater.*, 2020, **8**, 2001431.

70 (a) N. S. Makarov, S. Guo, O. Isaienko, W. Liu, I. Robel and V. I. Klimov, *Nano Lett.*, 2016, **16**, 2349–2362; (b) J. Fu, Q. Xu, G. Han, B. Wu, C. H. A. Huan, M. L. Leek and T. C. Sum, *Nat. Commun.*, 2017, **8**, 1300; (c) M. B. Price, J. Butkus, T. C. Jellicoe, A. Sadhanala, A. Briane, J. E. Halpert, K. Broch, J. M. Hodgkiss, R. H. Friend and F. Deschler, *Nat. Commun.*, 2015, **6**, 8420; (d) M. E. Madjet, G. R. Berdiyorov, F. El-Mellouhi, F. H. Alharbi, A. V. Akimov and S. Kais, *J. Phys. Chem. Lett.*, 2017, **8**, 4439–4445.

71 L. Ni, U. Huynh, A. Cheminal, T. H. Thomas, R. Shivanna, T. F. Hinrichsen, S. Ahmad, A. Sadhanala and A. Rao, *ACS Nano*, 2017, **11**, 10834.

72 Q. Du, C. Zhu, Z. Yin, G. Na, C. Cheng, Y. Han, N. Liu, X. Niu, H. Zhou and H. Chen, *ACS Nano*, 2020, **14**, 5806–5817.

73 S.-F. Zhang, X.-K. Chen, A.-M. Ren, H. Li and J.-L. Bredas, *ACS Energy Lett.*, 2018, **4**, 17–25.

74 J. Yin, P. Maity, R. Naphade, B. Cheng, J. H. He, O. M. Bakr, J. L. Bredas and O. F. Mohammed, *ACS Nano*, 2019, **13**, 12621–12629.

75 Y. Han, J. Yin, G. Cao, Z. Yin, Y. Dong, R. Chen, Y. Zhang, N. Li, S. Jin, O. F. Mohammed, B.-B. Cui and Q. Chen, *ACS Energy Lett.*, 2021, 453.

76 J. Luo, X. Wang, S. Li, J. Liu, Y. Guo, G. Niu, L. Yao, Y. Fu, L. Gao and Q. Dong, *Nature*, 2018, **563**, 541.

77 R. Zeng, L. Zhang, Y. Xue, B. Ke, Z. Zhao, D. Huang, Q. Wei, W. Zhou and B. Zou, *J. Phys. Chem. Lett.*, 2020, **11**, 2053.

78 K. M. McCall, C. C. Stoumpos, S. S. Kostina, M. G. Kanatzidis and B. W. Wessels, *Chem. Mater.*, 2017, **29**, 4129.

79 H. Siddique, Z. Xu, X. Li, S. Saeed, W. Liang, X. Wang, C. Gao, R. Dai, Z. Wang and Z. Zhang, *J. Phys. Chem. Lett.*, 2020, **11**, 9572.

80 S. Zelewski, J. Urban, A. Surrente, D. Maude, A. Kuc, L. Schade, R. Johnson, M. Dollmann, P. Nayak and H. Snaith, *J. Mater. Chem. C*, 2019, **7**, 8350.

81 T. Kirchartz, T. Markvart, U. Rau and D. A. Egger, *J. Phys. Chem. Lett.*, 2018, **9**, 939.

82 X. Lao, Z. Yang, Z. Su, Y. Bao, J. Zhang, X. Wang, X. Cui, M. Wang, X. Yao and S. Xu, *J. Phys. Chem. C*, 2019, **123**, 5128.

83 Y. Song, X. Zhang, L. Li, Z. Mo, J. Xu, S. Yu, X. Liu and J. Zhang, *Mater. Res. Express*, 2019, **6**, 115064.

84 S. Neutzner, F. Thouin, D. Cortecchia, A. Petrozza, C. Silva and A. R. S. Kandada, *Phys. Rev. Mater.*, 2018, **2**, 064605.

85 J. Li, H. Wang and D. Li, *Front. Optoelectron.*, 2020, 1–10.

86 C. Leung and K. Song, *Solid State Commun.*, 1980, **33**, 907.

87 M. Schulz and W. Von Der Osten, *Phys. Status Solidi*, 1993, **177**, 201.

88 M. Moreno, M. Barriuso and J. Aramburu, *J. Phys. Chem. Lett.*, 1992, **4**, 9481.

89 V. Türck, S. Rodt, O. Stier, R. Heitz, R. Engelhardt, U. Pohl, D. Bimberg and R. Steingrüber, *Phys. Rev. B: Condens. Matter Mater. Phys.*, 2000, **61**, 9944.

90 H. Zhao and H. Kalt, *Phys. Rev. B: Condens. Matter Mater. Phys.*, 2003, **68**, 125309.

91 R. Bartram, J. Charpie, L. J. Andrews and A. Lempicki, *Phys. Rev. B: Condens. Matter Mater. Phys.*, 1986, **34**, 2741.

92 S. Barman, N. Venkataraman, S. Vasudevan and R. Seshadri, *J. Phys. Chem. B*, 2003, **107**, 1875–1883.

93 D. G. Billing and A. Lemmerer, *Acta Crystallogr., Sect. B: Struct. Sci.*, 2007, **63**, 735–747.

94 A. Zeb, Z. Sun, A. Khan, S. Zhang and J. Luo, *Inorg. Chem. Front.*, 2018, **5**.

95 H. Abid, A. Trigui, A. Mlayah, E. K. Hlil and Y. Abid, *Results Phys.*, 2012, **2**, 71–76.

96 S. Wang, Y. Yao, J. Kong, S. Zhao, Z. Sun, Z. Wu, L. Li and J. Luo, *Chem. Commun.*, 2018, **54**, 4053–4056.

97 (*a*) Y. Shi, Z. Ma, D. Zhao, Y. Chen, Y. Cao, K. Wang, G. Xiao and B. Zou, *J. Am. Chem. Soc.*, 2019, **141**, 6504–6508; (*b*) R. Fu, W. Zhao, L. Wang, Z. Ma, G. Xiao and B. Zou, *Angew. Chem., Int. Ed.*, 2021, **60**, 10082–10088; (*c*) D. Zhao, G. Xiao, Z. Liu, L. Sui, K. Yuan, Z. Ma and B. Zou, *Adv. Mater.*, 2021, 2100323; (*d*) M. E. Sun, T. Geng, X. Yong, S. Lu, L. Ai, G. Xiao, J. Cai, B. Zou and S. Q. Zang, *Adv. Sci.*, 2021, **8**, 2004853.

98 (*a*) Y. Jing, Y. Liu, X. Jiang, M. S. Molokeev, Z. Lin and Z. Xia, *Chem. Mater.*, 2020, **32**, 5327–5334; (*b*) P. Han, C. Luo, S. Yang, Y. Yang, W. Deng and K. Han, *Angew. Chem., Int. Ed.*, 2020, **59**, 12709–12713; (*c*) Y. Zhou, J. Chen, O. M. Bakr and H.-T. Sun, *Chem. Mater.*, 2018, **30**, 6589–6613.

99 (*a*) W. Liu, Q. Lin, H. Li, K. Wu, I. Robel, J. M. Pietryga and V. I. Klimov, *J. Am. Chem. Soc.*, 2016, **138**, 14954–14961;

(*b*) A. Swarnkar, W. J. Mir and A. Nag, *ACS Energy Lett.*, 2018, **3**, 286–289; (*c*) J.-H. Wei, J.-F. Liao, X.-D. Wang, L. Zhou, Y. Jiang and D.-B. Kuang, *Matter*, 2020, **3**, 892–903.

100 X. Cheng, L. Jing, Y. Yuan, S. Du, Q. Yao, J. Zhang, J. Ding and T. Zhou, *CrystEngComm*, 2019, **21**, 4085–4091.

101 X.-F. Sun, P.-F. Li, W.-Q. Liao, Z. Wang, J. Gao, H.-Y. Ye and Y. Zhang, *Inorg. Chem.*, 2017, **56**, 12193–12198.

102 M. Li, J. Zhou, G. Zhou, M. S. Molokeev, J. Zhao, V. Morad, M. V. Kovalenko and Z. Xia, *Angew. Chem., Int. Ed.*, 2019, **58**, 18670–18675.

103 S. K. Dutta, A. Dutta, S. Das Adhikari and N. Pradhan, *ACS Energy Lett.*, 2019, **4**, 343–351.

104 C. Zhou, H. Lin, Y. Tian, Z. Yuan, R. Clark, B. Chen, L. J. van de Burgt, J. C. Wang, Y. Zhou, K. Hanson, Q. J. Meisner, J. Neu, T. Besara, T. Siegrist, E. Lambers, P. Djurovich and B. Ma, *Chem. Sci.*, 2018, **9**, 586–593.

105 K.-z Du, X. Wang, Q. Han, Y. Yan and D. B. Mitzi, *ACS Energy Lett.*, 2017, **2**, 2486–2490.

106 X. Cheng, L. Jing, Y. Yuan, S. Du, J. Zhang, X. Zhan, J. Ding, H. Yu and G. Shi, *J. Phys. Chem. C*, 2019, **123**, 1669–1676.

107 J.-H. Wei, J.-F. Liao, L. Zhou, J.-B. Luo, X.-D. Wang and D.-B. Kuang, *Sci. Adv.*, 2021, **7**, eabg3989.

108 Y. Zhang, X. Liu, H. Sun, J. Zhang, X. Gao, C. Yang, Q. Li, H. Jiang, J. Wang and D. Xu, *Angew. Chem., Int. Ed.*, 2021, **60**, 7587–7592.

109 J. Zhou, Z. Xia, M. S. Molokeev, X. Zhang, D. Peng and Q. Liu, *J. Mater. Chem. A*, 2017, **5**, 15031–15037.

110 L.-J. Xu, S. Lee, X. Lin, L. Ledbetter, M. Worku, H. Lin, C. Zhou, H. Liu, A. Plaviak and B. Ma, *Angew. Chem., Int. Ed.*, 2020, **59**, 14120–14123.

111 Z. Li, G. Song, Y. Li, L. Wang, T. Zhou, Z. Lin and R.-J. Xie, *J. Phys. Chem. Lett.*, 2020, **11**, 10164–10172.

112 Y. Jing, Y. Liu, J. Zhao and Z. Xia, *J. Phys. Chem. Lett.*, 2019, **10**, 7439–7444.